






# RIS-Aided Radar for Target Detection: Clutter Region Analysis and Joint Active-Passive Design

Zhuang Xie , Linlong Wu , *Senior Member, IEEE*, Jiahua Zhu , *Senior Member, IEEE*,  
 Marco Lops , *Fellow, IEEE*, Xiaotao Huang, *Senior Member, IEEE*,  
 and M. R. Bhavani Shankar , *Senior Member, IEEE*

**Abstract**—Reconfigurable Intelligent Surface (RIS) brings a transformative potential to radar systems by providing a new dimension to control electromagnetic waves. This paper focuses on enhancing target detectability through the design and analysis of RIS-aided radar. A comprehensive signal model is established, recognizing both Line of Sight (LoS) and Non-Line of Sight (N-LoS) returns, factoring in RIS location and range gate shifts. This modeling enables an examination of the RIS-dependent effect of enlarged clutter region, underscoring the essential need for precise RIS phase optimization. A joint design problem encompassing transmit waveform, receive filter, and RIS phase is then formulated with the aim to optimize Signal-to-Interference-plus-Noise-Ratio (SINR), complying with practical waveform constraints and discrete RIS phase alphabet. For this nonconvex problem, an iterative algorithm is developed to monotonically enhance SINR, ensuring convergence by alternately updating the radar waveform and RIS phases. Through the majorization-minimization framework, radar waveform updates are achieved using the feasible point pursuit technique, while a quasi-closed form solution is employed for the RIS phases. Simulation results demonstrate the efficacy of the proposed design, revealing the crucial role of RIS in the system.

**Index Terms**—Reconfigurable Intelligent Surface (RIS), target detection, waveform design, Non-Line of Sight (N-LoS), majorization-minimization.

## I. INTRODUCTION

RECONFIGURABLE Intelligent Surfaces (RISs) are planar structures consisting of a series of reflective units - made of metamaterials - which can change the amplitude and/or the phases of an incoming signal with little or no power consumption [1], [2], [3], [4]. Proper deployment of an RIS may henceforth yield a viable means to “reshape” the communication channel, thus enhancing the reliability of wireless services and the efficiency of resource utilization.

### A. Related Work

Current research on RIS mainly focuses on exploring its potential to improve various Quality of Service (QoS) in wireless communication applications. In [5], the fundamental capacity limit of point-to-point RIS-aided Multiple-Input-Multiple-Output (MIMO) systems is enhanced by jointly optimizing the RIS phase shifts and MIMO transmit autocorrelation matrix. For a RIS-aided Multiple-Input-Single-Output (MISO) system, preliminary results on optimizing the phase shifts to maximize the ergodic spectral efficiency are provided in [6], where a closed-form solution to the resulting optimization problem is given. In [7], the communication scenario between multi-antenna base station and single-antenna multiple users aided by RIS is considered, and the transmit power is minimized under Signal-to-Interference-plus-Noise-Ratio (SINR) constraints by joint design of active and passive beamforming. Concerning practical hardware limitation, [8] extends the work in [7] to the case where the RIS phase shifts are only allowed to vary in a discrete alphabet. In the context of RIS-aided point-to-point MIMO links, [9] reduces the bit error rate through joint optimization of transmit coding and RIS phase shifts. The channel estimation task with the assistance of RIS is investigated in [10]. In [11], the physical layer security issue of Single-Input-Multiple-Output (SIMO) transmission with the assistance of RIS is considered, where receive beamforming, active jamming, and RIS-aided beamforming are jointly optimized to achieve enhanced security performance. Assuming propagation blockage between the users and base station, [12] uses RIS to create a linking path and jointly optimize base station

Manuscript received 15 August 2023; revised 16 January 2024 and 17 February 2024; accepted 20 February 2024. Date of publication 28 February 2024; date of current version 5 April 2024. The work of Zhuang Xie, Jiahua Zhu, and Xiaotao Huang was supported in part by the National Natural Science Foundation of China under Grant 62101573, and the scientific research project of National University of Defense Technology under Grant ZK20-35. The work of Linlong Wu and M. R. Bhavani Shankar was supported in part by the FNR CORE INTER Project SENCOM under Grant C20/IS/14799710/SENCOM and in part by the FNR CORE Project S3 under Grant C22/IS/17412681/S3. The work of Marco Lops was supported in part by the European Union under Italian National Recovery and Resilience Plan (NRRP) of NextGenerationEU, partnership on “Telecommunications of the Future” (PE00000001-Program “RESTART”) under Grant E63C22002040007. The associate editor coordinating the review of this manuscript and approving it for publication was Prof. Mojtaba Soltanalian. (Corresponding authors: Linlong Wu; Xiaotao Huang.)

Zhuang Xie and Xiaotao Huang are with the College of Electronic Science and Technology, National University of Defense Technology, Changsha 410000, China (e-mail: xiezhuang18@nudt.edu.cn; xthuang@nudt.edu.cn).

Linlong Wu and M. R. Bhavani Shankar are with Interdisciplinary Centre for Security, Reliability and Trust (SnT), University of Luxembourg, 4365 Esch-sur-Alzette, Luxembourg (e-mail: linlong.wu@uni.lu; bhavani.shankar@uni.lu).

Jiahua Zhu is with the College of Meteorology and Oceanography, National University of Defense Technology, Changsha 410073, China (e-mail: zhujiahua1019@hotmail.com).

Marco Lops is with the Department of Electrical and Information Technology, University of Naples Federico II, 80138 Naples, Italy, and also with Consorzio Nazionale Interuniversitario per le Telecomunicazioni, 43124 Parma, Italy (e-mail: lops@unina.it).

Digital Object Identifier 10.1109/TSP.2024.3371292

transmit beamforming and RIS phase shifts from a deep reinforcement learning perspective to maximize the ergodic sum rate of downlink links in multi-user MISO systems. In addition to the above-mentioned works, RIS deployment has been advocated as a viable means to improve Dual-Functional Radar-Communication (DFRC) systems, where the radar may benefit from the RIS's present in the scene [13], [14], [15], [16], [17], [18], [19], [20], [21], [22].

Undoubtedly, as a novel means to affect the propagation channel, RIS brings new Degrees of Freedom (DoF) to the optimization of a wireless propagation system. Although RIS was originally proposed and well-studied in wireless communications, its ability to influence signal propagation indicates its potentials in assisting radar operations, as suggested by some early contributions concerning radar detection in traditional [23] and distributed MIMO [24] architectures. The study [25] considers the influence of signal bandwidth, carrier frequency, and the size and relative position of RIS, radar, and targets on the signal model and provides preliminary suggestions on the deployment scheme of RIS for target detection tasks. The work [26] further generalizes the work in [25] to the MIMO radar situation, coming to the conclusion that RIS should be in close proximity to radar transceivers. The contribution [27], instead, proposes the exploitation of a suitably placed RIS to generate Non-Line of Sight (N-LoS) paths. A multi-target scenario is considered in [28], stating and solving a power allocation problem - along with joint design of radar beamformer and RIS phase shifts - as multiple RISs are present in the scene, while the issue of sidelobe control is tackled in [29] with reference to an active RIS-assisted monostatic radar. The possibility of emulating a MIMO radar by incorporating an illuminator and a RIS is verified in [30], where the beampattern is designed in the space-frequency domain through the design of source signals and RIS phases. On parallel tracks, the potentials of RIS deployment in target parameter estimation has also been recently explored [31], [32], [33].

Notice that early studies on RIS-aided radars regard an RIS as a mirror able to re-focus an impinging pre-determined signal to a given point of the space. A definitely more attractive approach is to regard the radar transmitter and the RIS as a unique system, so that the transmitted waveform and the RIS phase shifts are jointly designed in order to optimize the chosen figure of merit [34], [35], [36], [37]. Such an idea has been applied to the detection of multiple targets in RIS-assisted architectures in [34], where in the RIS phase shifts and radar waveform are jointly optimized under a constraint on the transmit energy and assuming that no clutter (i.e., signal-dependent reverberation) affects the received signal. Clutter is instead accounted for in [35], [36], wherein, the RIS phase shifts are assumed to vary in a continuous alphabet, which is in some contradiction with RIS hardware limitations.

### B. Motivation of This Work

The present contribution is aimed at shedding some light on the interplay between RIS and clutter: in principle, it is indeed inevitable that the clutter undergoes the same effect as the useful signal, whereby a RIS would inevitably scatter towards the

radar receiver also the echo from random scatters populating the scene. Thus both the target and clutter centers produce LoS and N-LoS returns, which are inevitably not range-aligned due to the different propagation paths.

For example, suppose a monostatic radar with 3 GHz carrier frequency is aided by a 64-element RIS with half-wavelength element spacing, the radar bandwidth is 50 MHz and pulse duration is 1  $\mu$ s (lead to 20 subpulses), the target is located 5 km far from radar and the distance between radar and RIS center is 100 m, the angle formed by linking target, radar and RIS center is 70°. In this case, the range gate shift of the N-LoS path compared with the LoS path reaches 16 units (i.e., 80% of the entire pulse). Moreover, due to the N-LoS propagation, the behavior of the signal-dependent clutter can be distinctly more complicated, as will be shown in this paper. Therefore, it is essential to optimally utilize the DoF at both the radar and RIS ends under a more general and practical model to resolve the above introduced issues.

### C. Contributions of This Work

In detail, the main contributions of this paper are summarized as follows:

1) *We Present a General Signal Model for RIS-Aided Radar Systems in Clutter:* We establish an articulated signal model for RIS-aided radar, accounting for the strict relationship between phase and range gate shift among various returns. Such model can account for scenarios where signals from both LoS and N-LoS paths are resolvable in the time domain. Leveraging the model, we introduce and investigate the extricate effect of enlarged clutter region that emerges when integrating RIS into conventional radar systems. Our analysis reveals that, in addition to careful selection of RIS location, both the radar transmit waveform and RIS phase shifts must be judiciously designed to overcome the Signal-to-Clutter Ratio (SCR) degeneration caused by the aforementioned effect.

2) *We Offer a Practical Formulation for Joint Radar-RIS Design in Target Detection:* From the point of view of system design, we exploit the design DoF at both radar and RIS ends to maximize the SINR: in our setup, this amounts to jointly designing the transmit waveform, the receive filter and the phase shifts of the RIS. In particular, we constrain the radar waveform to possess constant modulus, on top of meeting constraints on similarity with some standard radar waveforms and spectral compatibility. We also assume the RIS phase shifts to belong to a finite alphabet, which is a key hardware limitation in RIS realization.

3) *We Design and Assess an Effective Algorithm to Tackle the Non-Convex Joint Design Problem:* We develop an effective optimization algorithm, each iteration of which involves the alternating update of radar waveform and RIS phase shifts, respectively. For the subproblem of the radar waveform, by adopting the Majorization-Minimization (MM) framework in conjunction with the Feasible Point Pursuit (FPP) technique, we find a suboptimal solution satisfying the Karush-Kuhn-Tucker (KKT) conditions. For the subproblem of RIS phases, our derivations indicate that it can be tackled by solving a series of non-convex optimizations, admitting quasi-closed-form

TABLE I  
GLOSSARY OF NOTATIONS

Notations	Description	Notations	Description
$G_t$	Beam gain towards target.	$\dot{\sigma}^E$	Expectation of target RCS.
$G_{\text{RIS},n}$	Beam gain towards $n$ -th element of RIS.	$\dot{\varphi}$	Target LoS return phase.
$d_{r,t}$	Distance between radar and target.	$\dot{\varphi}_n$	Target N-LoS return phase (through RIS $n$ -th element).
$d_{r,n}$	Distance between radar and $n$ -th element of RIS.	$\ddot{\alpha}_k$	LoS channel propagation coefficient of $k$ -th scatterer.
$d_r$	Distance between radar and RIS center.	$d_{r,c,k}$	Distance between radar and $k$ -th scatterer.
$d_{t,n}$	Distance between target and $n$ -th element of RIS.	$G_{c,k}$	Beam gain towards $k$ -th scatterer.
$d_t$	Distance between target and RIS center.	$\ddot{\sigma}_k$	RCS of $k$ -th scatterer.
$d_{\text{RIS}}$	Inter-element spacing of RIS array.	$\psi_k$	Phase of $k$ -th scatterer.
$\theta_t^{\text{RIS}}$	Direction of target w.r.t the RIS array.	$\dot{\varphi}_k$	LoS delay of $k$ -th scatterer.
$\theta_{t,r,\text{RIS}}$	Angle formed by radar-RIS center and radar-target.	$\dot{\varphi}_{k,n}$	N-LoS delay of $k$ -th scatterer (through RIS $n$ -th element).
$D_{\text{RIS}}$	RIS	$d_{c,k,n}$	Distance between $k$ -th scatterer and $n$ -th element of RIS.
$D_t$	Target size.	$f_s$	Radar sampling frequency.
$\dot{r}_n$	Range gate shift of target N-LoS return (through RIS $n$ -th element).	$\ddot{\alpha}_{k,n}$	N-LoS channel propagation coefficient of $k$ -th scatterer return (through RIS $n$ -th element).
$r_{\text{data}}$	Length of data containing target information.	$\ddot{r}_k$	Range gate shift of $k$ -th scatterer LoS return.
$\dot{\alpha}$	LoS channel propagation coefficient of target.	$\dot{\sigma}_k^E$	Expectation of $k$ -th scatterer RCS.
$\dot{\alpha}_n$	Target N-LoS channel propagation coefficient (through RIS $n$ -th element).	$\ddot{r}_{k,n}$	Range gate shift of $k$ -th scatterer N-LoS return (through RIS $n$ -th element).
$P$	Radar transmit power.	$\dot{\sigma}_{\text{RIS},n}$	RCS of RIS $n$ -th element radiated from target.
$\dot{\sigma}$	Target RCS.	$\dot{\sigma}_{\text{RIS},k,n}$	RCS of RIS $n$ -th element radiated from $k$ -th scatterer.
$\dot{\psi}$	Target phase.		

solutions. Furthermore, we discuss the initialization of our derived algorithm and analyze its convergence and complexity.

4) *Simulation Validation and Analysis*: Through extensive simulations, we demonstrate the benefits of the RIS-aided radar architectures in the presence of clutter, offering a thorough analysis of the interplay among the system parameters. Of course, this performance boost is not universally guaranteed with a mere RIS deployment. Our simulation indicates that unwise RIS phases design may severely undermine the original radar functionality, which highlights the importance of a comprehensive design approach when integrating RIS into radar systems.

The remainder of this paper is organized as follows. Section II establishes the signal model for RIS-aided radar system. Section III formulates the joint design problem of radar transmit waveform, receive filter and RIS phase shifts. Section IV develops a novel algorithm to enhance the SINR of RIS-aided radar while guaranteeing complex waveform properties and polyphase shifts. Numerical experiments and analyses are given in Section V. Finally, in Section VI, conclusions are drawn.

*Notations*:  $(\cdot)^T$ ,  $(\cdot)^*$ ,  $(\cdot)^\dagger$  denote transpose, conjugate and conjugate transpose, respectively.  $\mathbb{C}^N$  is the set of  $N$ -dimensional complex space.  $\Re\{\cdot\}$  and  $\arg(\cdot)$  obtains the real part and the phase of a complex argument, respectively.  $\mathbb{E}\{\cdot\}$  is the expectation operator. For a Hermitian matrix  $\mathbf{A}$ ,  $\mathbf{A} \succeq 0$  means  $\mathbf{A}$  is positive semi-definite.  $\mathbf{I}_N$  denotes  $N \times N$ -dimensional identity matrix.  $\lceil a \rceil$  provides the lowest integer no smaller than the real number  $a$ . The readers' easy reference, the main notations utilized is tabulated in Table I.

## II. RIS-AIDED MONOSTATIC RADAR: SIGNAL MODEL AND ANALYSIS

In this section, we will first establish a detailed signal model for RIS-aided radar, where a strict relationship between the

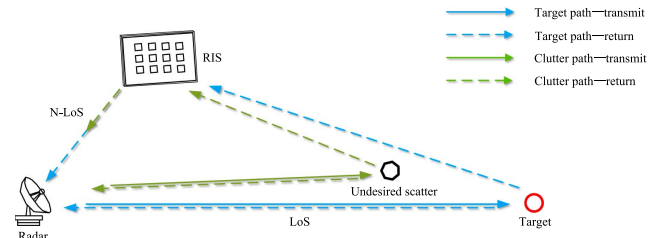


Fig. 1. Pictorial representation of the operation scene where a RIS is deployed to aid the radar.

phases and range gate shifts are accounted. Based on the model, we discuss its generality by extending it to the multipulse case in Section II-B. Furthermore, we introduce and investigate the effect of RIS-dependent clutter region in Section II-C.

### A. Signal Model for the Monopulse Case

As shown in Fig. 1, a monostatic radar is aided by an  $N$ -element RIS deployed in the scene to detect targets in the presence of some strong scatters. Suppose that the radar possesses one transmit beam pointing towards the target, and two receive beams pointing towards the target and the RIS<sup>1</sup>, respectively. The radar transmits a pulse signal coded by the waveform vector  $\mathbf{s} = [s_1, s_2, \dots, s_L]^T \in \mathbb{C}^L$ , where  $L$  is the fast-time sample number. Assume that the radar beam gains towards the target and the  $n$ -th RIS element are  $G_t$  and  $G_{\text{RIS},n}$ , respectively. Denote the distances between radar and target, radar and  $n$ -th element (array center) of RIS, target and  $n$ -th element (array center) of RIS by  $d_{r,t}$ ,  $d_{r,n}$  ( $d_r$ ) and  $d_{t,n}$  ( $d_t$ ), respectively. Without loss of generality, it is assumed that

<sup>1</sup>With reference to real implementation, such requirement can be realized by utilizing a phased array or an antenna with good directivity [25], [38].

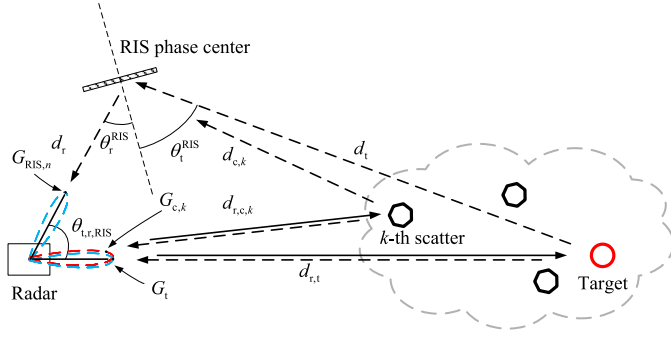


Fig. 2. Illustration of the parameters involved in the RIS-aided scene.

$N$  is an odd number. As depicted in Fig. 2, we have  $d_{t,n} = d_t + (n - \frac{N+1}{2}) d_{\text{RIS}} \sin \theta_t^{\text{RIS}}$  based on the far-field assumption, where  $d_{\text{RIS}}$  is the spacing between the RIS reflecting units and  $\theta_t^{\text{RIS}}$  is the direction of the target w.r.t the RIS array. Denoting  $\theta_{t,r,\text{RIS}}$  the angle formed by the two receive beams (i.e., the radar-target and the radar-RIS directions), it follows that  $d_t = \sqrt{d_{r,t}^2 + d_r^2 - 2d_{r,t}d_r \cos \theta_{t,r,\text{RIS}}}$ .

Fig. 2 highlights the relationships of the diverse system parameters. Before proceeding further, we make the following assumptions and considerations:

- The RIS is deployed relatively close to the radar, compared with its far distance from the target, i.e., RIS is in the far-field of the target ( $\min\{d_{t,n}\}_{n=1}^N \geq \frac{2 \max\{D_{\text{RIS}}^2, D_t^2\}}{\lambda}$  with  $D_{\text{RIS}}$  and  $D_t$  being the size of RIS and target<sup>2</sup>).
- The RIS position and orientation with respect to the radar are known in advance and can be treated as prior information.
- For target and clutter centers, the Radar Cross Section (RCS) from the LoS path and the N-LoS path are identical.
- The N-LoS returns of the target overlap with the LoS return at some range gates. Mathematically, this relationship can be expressed as  $\min_n \{\dot{r}_n\} < L$ ,  $n = 1, 2, \dots, N$ , where  $\dot{r}_n = \left\lceil \frac{(d_{r,n} + d_{t,n} + d_{r,t})f_s}{c} \right\rceil - \left\lceil \frac{2d_{r,t}f_s}{c} \right\rceil$  is the range gate delay between the N-LoS path (through the  $n$ -th element of the RIS) and the LoS path of target return<sup>3</sup>,  $f_s$  is the fast time sampling frequency of radar system and  $c$  is the speed of light.

The echo data at the receiver end after down-conversion and digital sampling can be given as

$$\mathbf{y} = \mathbf{y}_t + \mathbf{y}_c + \mathbf{n} \in \mathbb{C}^{r_{\text{data}}}, \quad (1)$$

where  $\mathbf{y}_t$  is the target return component,  $\mathbf{y}_c$  is the signal-dependent clutter item that contributes to  $\mathbf{y}$ ,  $\mathbf{n} \sim \mathcal{CN}(\mathbf{0}, \mathbf{R}_n)$  is the signal-independent disturbance accounting for the noise and interfering signals,  $r_{\text{data}} = \max_n \{\dot{r}_n\} + L$  indicates the length

<sup>2</sup>The benefit of RIS's close placement w.r.t the radar is supported by the conclusion given in [25], [26]. Moreover, from applicability perspective, it is justified to deploy RIS nearby radar platform in a target surveillance mission.

<sup>3</sup>We utilize diacritical marks ( $\dot{\cdot}$ ) and ( $\ddot{\cdot}$ ) to distinguish between the target and clutter related parameters, respectively.

of data containing target information since the target return from LoS and N-LoS path are distributed in different range gates.

The signal from the target  $\mathbf{y}_t$  is composed of an LoS and an N-LoS component, the latter reflected from the RIS. Thus,  $\mathbf{y}_t$  is further written as

$$\begin{aligned} \mathbf{y}_t &= \sqrt{\dot{\sigma}} e^{j\dot{\psi}} \left( \dot{\alpha} e^{j\dot{\varphi}} \mathbf{J}_0 + \sum_{n=1}^N \dot{\alpha}_n \phi_n e^{j\dot{\varphi}_n} \mathbf{J}_{\dot{r}_n} \right) \mathbf{s} \\ &= \sqrt{\dot{\sigma}} e^{j\dot{\psi}} \mathbf{H}_t(\phi) \mathbf{s} \in \mathbb{C}^{r_{\text{data}}}, \end{aligned} \quad (2)$$

where  $\dot{\alpha} = \sqrt{\frac{PG_t^2 \lambda^2}{(4\pi)^3 d_{r,t}^4}}$  and  $\dot{\alpha}_n = \sqrt{\frac{PG_t G_{\text{RIS},n} \lambda^2 \dot{\sigma}_{\text{RIS},n}}{(4\pi)^4 d_{r,t}^2 d_{t,n}^2 d_r^2}}$  are the channel propagation coefficient of the LoS and of the N-LoS path, respectively,  $P$  is the radar transmit power,  $\sqrt{\dot{\sigma}} e^{j\dot{\psi}}$  is the target complex backscattering coefficient with  $\dot{\sigma}$  being the RCS and  $\dot{\psi}$  being the phase,  $\dot{\sigma}_{\text{RIS},n}$  stands for the RCS of the RIS  $n$ -th element radiated from the target,  $\dot{\varphi} = -4\pi \frac{d_{r,t}}{\lambda}$  and  $\dot{\varphi}_n = -2\pi \frac{d_{r,t} + d_{r,n} + d_{r,n}}{\lambda}$  with  $\lambda$  being the wavelength of the transmit waveform. The matrix  $\mathbf{H}_t(\phi)$  is

$$\mathbf{H}_t(\phi) = \dot{\alpha} e^{j\dot{\psi}} \mathbf{J}_0 + \sum_{n=1}^N \dot{\alpha}_n \phi_n e^{j\dot{\varphi}_n} \mathbf{J}_{\dot{r}_n}, \quad (3)$$

where  $\phi = [\phi_1, \phi_2, \dots, \phi_N]^T \in \mathbb{C}^N$  is defined as Reflection Coefficient Vector (RCV) with  $\phi_n$  being its  $n$ -th element, and  $\mathbf{J}_r \in \mathbb{C}^{r_{\text{data}} \times L}$  is the shift matrix

$$\mathbf{J}_r(m, n) = \begin{cases} 1, & m - n - r = 0 \\ 0, & m - n - r \neq 0 \end{cases}. \quad (4)$$

Let us now consider the signal-dependent echo  $\mathbf{y}_c$  introduced by clutter centers embedding the target. Suppose there are  $K$  undesired scatters, then  $\mathbf{y}_c = \sum_{k=1}^K \mathbf{y}_{c,k}$  with  $\mathbf{y}_{c,k}$  being the return from the  $k$ -th scatterer. The  $k$ -th return  $\mathbf{y}_{c,k}$  can be further expressed as

$$\begin{aligned} \mathbf{y}_{c,k} &= \sqrt{\ddot{\sigma}_k} e^{j\ddot{\psi}_k} \left( \ddot{\alpha}_k e^{j\ddot{\varphi}_k} \mathbf{J}_{\ddot{r}_k} + \sum_{n=1}^N \ddot{\alpha}_{k,n} \phi_n e^{j\ddot{\varphi}_{k,n}} \mathbf{J}_{\ddot{r}_{k,n}} \right) \mathbf{s} \\ &= \sqrt{\ddot{\sigma}_k} e^{j\ddot{\psi}_k} \mathbf{H}_{c,k}(\phi) \mathbf{s} \in \mathbb{C}^{r_{\text{data}}}, \end{aligned} \quad (5)$$

where  $\ddot{\alpha}_k = \sqrt{\frac{PG_{c,k}^2 \lambda^2}{(4\pi)^3 d_{r,c,k}^4}}$  with  $d_{r,c,k}$  the distance between the radar and the  $k$ -th scatterer and  $G_{c,k}$  the radar beam gain towards the  $k$ -th clutter center,  $\sqrt{\ddot{\sigma}_k} e^{j\ddot{\psi}_k}$  stands for the complex backscattering coefficient of  $k$ -th scatterer with  $\ddot{\sigma}_k$  and  $\ddot{\psi}_k$  accounting for the RCS and phase,  $\ddot{\varphi}_k = -4\pi \frac{d_{r,c,k}}{\lambda}$ ,  $\ddot{\varphi}_{k,n} = -2\pi \frac{d_{c,k,n} + d_{r,n} + d_{r,c,k}}{\lambda}$ ,  $d_{c,k,n}$  represents the distance between the  $k$ -th scatterer and the  $n$ -th element of RIS,  $\ddot{\alpha}_{k,n} = \sqrt{\frac{PG_{c,k} G_{\text{RIS},n} \lambda^2 \ddot{\sigma}_{\text{RIS},k,n}}{(4\pi)^4 d_{r,c,k}^2 d_{r,n}^2 d_r^2}}$  with  $\ddot{\sigma}_{\text{RIS},k,n}$  being the RCS of RIS  $n$ -th element radiated from  $k$ -th scatterer,  $\ddot{r}_k = \left\lceil \frac{2d_{r,c,k}f_s}{c} \right\rceil - \left\lceil \frac{2d_{r,t}f_s}{c} \right\rceil$  and  $\ddot{r}_{k,n} = \left\lceil \frac{(d_{c,k,n} + d_{r,n} + d_{r,c,k})f_s}{c} \right\rceil - \left\lceil \frac{2d_{r,t}f_s}{c} \right\rceil$  are the range gate delays from LoS path and N-LoS path (through the  $n$ -th element of RIS) compared with the target LoS path,  $\mathbf{H}_{c,k}(\phi) = \ddot{\alpha}_k e^{j\ddot{\varphi}_k} \mathbf{J}_{\ddot{r}_k} + \sum_{n=1}^N \ddot{\alpha}_{k,n} \phi_n e^{j\ddot{\varphi}_{k,n}} \mathbf{J}_{\ddot{r}_{k,n}}$ .



Substituting the above expressions into (1), we have

$$\begin{aligned} \mathbf{y}(\phi, \mathbf{s}) &= \mathbf{y}_t + \sum_{k=1}^K \mathbf{y}_{c,k} + \mathbf{n} \\ &= \sqrt{\sigma} e^{j\psi} \mathbf{H}_t(\phi) \mathbf{s} + \sum_{k=1}^K \sqrt{\sigma_k} e^{j\psi_k} \mathbf{H}_{c,k}(\phi) \mathbf{s} + \mathbf{n}. \end{aligned} \quad (6)$$

Direct inspection of (6) reveals the following facts:

- Compared with the signal model of traditional radar systems, the propagation environment may be reshaped through a wise selection of  $\phi$ , so as to take advantage of the N-LoS return for performance enhancement.
- The structure of the matrix  $\mathbf{H}_t(\phi)$  indicates clearly that the role of RIS is not only the RCV  $\phi$ , but also the  $d_{r,t}$  and  $d_{t,n}$  play an important role at the system design stage.
- Furthermore, the model considers explicitly the range gate shift caused by the RIS-introduced N-LoS propagation, which enable us to investigate quantitatively the range gate overlapping between the N-LoS and LoS returns and the effect of enlarged clutter region. This issue has not been considered in the models presented in the literature, and we will investigate it in Section II-C.

### B. Extension to the Multipulse Case

The above model can be extended to the multi-pulse scenarios, as concisely outlined in this subsection. Assume that the radar transmits  $M$  pulses to detect a moving target with velocity  $\dot{\mathbf{v}}$ . Denote by  $\hat{\theta}$  the included angle between  $\dot{\mathbf{v}}$  and  $\overrightarrow{TR}$ , and  $\hat{\theta}'$  the included angle between  $\dot{\mathbf{v}}$  and  $\overrightarrow{TS}$ , where  $\overrightarrow{TS}$  and  $\overrightarrow{TR}$  are unit vectors along target-radar and target-RIS directions, respectively. At the  $m$ -th pulse, denote by the modulus of  $\dot{\mathbf{v}}$  as  $\dot{v}$ , the target return at the receive end can be expressed as

$$\begin{aligned} \mathbf{y}_{t,p}^d &= \sqrt{\sigma} e^{j\psi} \left( \dot{\alpha} e^{j\psi} \mathbf{J}_0 e^{j\dot{v}(m-1)T_r} \right. \\ &\quad \left. + \sum_{n=1}^N \dot{\alpha}_n \phi_n e^{j\dot{v}'(m-1)T_r} e^{j\dot{v}_n} \mathbf{J}_{\dot{r}_n} \right) \mathbf{s}_m, \end{aligned}$$

where  $\mathbf{s}_m$  stands for the baseband waveform emitted by radar at  $m$ -th pulse and  $T_r$  represents the Pulse Repetition Time (PRT),  $\dot{f} = \frac{2\dot{v} \cos \hat{\theta}}{\lambda}$  and  $\dot{f}' = \frac{\dot{v}}{2} + \frac{\dot{v} \cos \hat{\theta}'}{\lambda}$  are the LoS and NLoS target Doppler frequency, respectively. Collecting all the  $M$  pulses into a vector yields

$$\begin{aligned} \mathbf{y}_t^d &= \sqrt{\sigma} e^{j\psi} \left( \dot{\alpha} e^{j\psi} (\dot{\mathbf{P}} \otimes \mathbf{J}_0) + \sum_{n=1}^N \dot{\alpha}_n \phi_n e^{j\dot{v}_n} (\dot{\mathbf{P}}' \otimes \mathbf{J}_{\dot{r}_n}) \right) \mathbf{s} \\ &= \sqrt{\sigma} e^{j\psi} \mathbf{H}_t^d(\phi) \mathbf{s}, \end{aligned} \quad (7)$$

where

$$\dot{\mathbf{P}} = \text{diag} \left\{ \left[ 1, e^{j\dot{f}T_r}, \dots, e^{j\dot{f}(M-1)T_r} \right]^T \right\}$$

and

$$\dot{\mathbf{P}}' = \text{diag} \left\{ \left[ 1, e^{j\dot{f}'T_r}, \dots, e^{j\dot{f}'(M-1)T_r} \right]^T \right\}$$

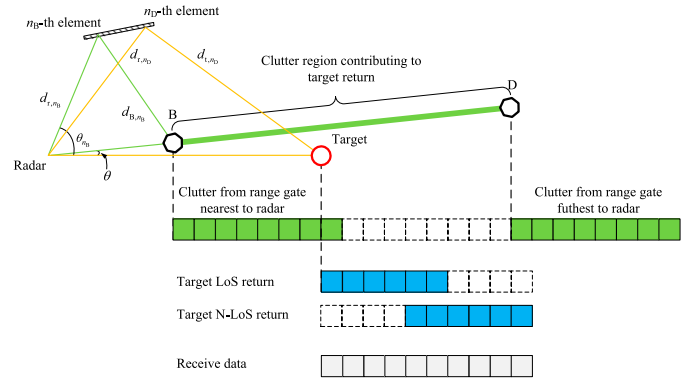


Fig. 3. The relationship between the contributing clutter and target return.

represent the Doppler steering matrices for LoS and N-LoS paths, respectively. The matrix  $\mathbf{H}_t^d(\phi)$  is given by

$$\mathbf{H}_t^d(\phi) = \dot{\alpha} e^{j\psi} (\dot{\mathbf{P}} \otimes \mathbf{J}_0) + \sum_{n=1}^N \dot{\alpha}_n \phi_n e^{j\dot{v}_n} (\dot{\mathbf{P}}' \otimes \mathbf{J}_{\dot{r}_n}). \quad (8)$$

The mathematical structure of  $\mathbf{H}_t^d(\phi)$  clearly reproduces that of  $\mathbf{H}_t(\phi)$  from the monopulse case (refer to Eq. (3)). Notably,  $\mathbf{H}_t^d(\phi)$  simplifies to  $\mathbf{H}_t(\phi)$  with just one transmitted pulse. In a similar vein, the clutter components in the multipulse scenario closely resemble those in the single-pulse case. Consequently, the multipulse signal model retains the mathematical structure of the single-pulse case, suggesting analogous SINR expressions in both. Our study, therefore, concentrates on the single-pulse case, on the understanding that the multi-pulse case can be easily derived with straightforward modifications.

### C. RIS-Dependent Clutter Region

Assuming the radar position as reference, the clutter contributions to the LoS path come from the range interval  $\left[ \left( -L + \lceil 2d_{r,t} \frac{f_s}{c} \rceil \right) \frac{c}{2f_s}, \left( L - 1 + \lceil 2d_{r,t} \frac{f_s}{c} \rceil \right) \frac{c}{2f_s} \right]$  contribute to the target return. In the presence of an RIS (see Fig. 3) extra returns contributing to the N-LoS paths with different propagation delays are generated, eventually resulting in an enlarged clutter region. The following proposition gives the expression of this clutter region.

*Proposition 1:* Taking the line linking radar and target as reference direction, the lower and upper boundaries of the contributing clutter region along direction  $\theta$  can be given as

$$\begin{cases} d_{r,B} = \frac{2d_{r,n_B} \frac{f_s}{c} - \lceil 2d_{r,t} \frac{f_s}{c} \rceil + L}{\left( \frac{d_{r,n_B} \cos(\hat{\theta}_{n_B} - \theta) + d_{r,n_B}}{\lceil 2d_{r,t} \frac{f_s}{c} \rceil \frac{c}{f_s} - L \frac{c}{f_s}} - 1 \right) 2f_s}, \\ d_{r,D} = \left( L - 1 + \lceil (d_{r,t} + d_{t,n_D} + d_{r,n_D}) \frac{f_s}{c} \rceil \right) \frac{c}{2f_s} \end{cases}, \quad (9)$$

where

$$\begin{cases} n_B = \arg \max_n \{d_{B',n} + d_{r,n}\} \\ n_D = \arg \max_n \{d_{t,n} + d_{r,n}\} \end{cases}. \quad (10)$$

In other words, the returns from scatters within  $(d_{r,B}, d_{r,D}]$  overlap with the target return at direction  $\theta$ .

*Proof:* See Appendix A. ■

*Remark:* Based on the fact that  $d_{r,n_B} \cos(\dot{\theta}_{n_B} - \theta) + d_{r,n_B} \leq 2d_{r,n_B}$  and  $d_{t,n_D} + d_{r,n_D} \geq d_{r,t}$ , a closer observation of (9) reveals that

$$\begin{cases} d_{r,B} \leq \left( -L + \lceil 2d_{r,t} \frac{f_s}{c} \rceil \right) \frac{c}{2f_s} \\ d_{r,D} \geq \left( L - 1 + \lceil 2d_{r,t} \frac{f_s}{c} \rceil \right) \frac{c}{2f_s} \end{cases} \quad (11)$$

stands. Such results indicate that the deployment of RIS actually enlarges the clutter region that contributes to the target return compared with the no-RIS case.

Therefore, although RIS brings extra information about the target through the target N-LoS return, additional clutter is also involved in the data to be processed. To provide more intuitive explanations of the clutter issue for RIS-aided radar, we now define the SCR at the receiver, whose expression is given as

$$\text{SCR} = \frac{\mathbb{E} \left\{ \|\mathbf{y}_t\|_2^2 \right\}}{\sum_{k=1}^K \mathbb{E} \left\{ \|\mathbf{y}_{c,k}\|_2^2 \right\}} = \frac{\dot{\sigma}^E \mathbf{s}^\dagger \mathbf{H}_t^\dagger(\phi) \mathbf{H}_t(\phi) \mathbf{s}}{\sum_{k=1}^K \ddot{\sigma}_k^E \mathbf{s}^\dagger \mathbf{H}_{c,k}^\dagger(\phi) \mathbf{H}_{c,k}(\phi) \mathbf{s}}, \quad (12)$$

where  $\dot{\sigma}^E = \mathbb{E} \{ \dot{\sigma} \}$ , and  $\mathbb{E} \left\{ \sqrt{\dot{\sigma}_{k_1}} \sqrt{\dot{\sigma}_{k_2}} \right\} = \ddot{\sigma}_{k_1}^E \delta_{k_1 k_2}$  with  $\ddot{\sigma}_k^E = \mathbb{E} \{ \ddot{\sigma}_k \}$  under the assumption of independent scatters<sup>4</sup>. To assess the impact of the clutter region size over the SCR, we rotate the 128-element RIS around the radar to change  $\theta_{t,r,\text{RIS}}$  from  $35^\circ$  to  $85^\circ$  while keeping the inclination of RIS placement direction w.r.t x-axis as  $30^\circ$  and  $d_r = 200$  m, as illustrated in Fig. 4. The resulting SCR and clutter region boundary behavior along target direction are plotted in Fig. 5, where a 32-length Linear Frequency Modulated (LFM) signal is chosen as the radar waveform and RIS phase shifts are randomly generated. It is clearly observed that as  $\theta_{t,r,\text{RIS}}$  varies from  $35^\circ$  to  $85^\circ$ , clutter from further scatters are involved due to the longer target data length. The results also reveal that the SCR exhibits a degradation behavior with the enlargement of the clutter region. This can be explained as follows: As  $\theta_{t,r,\text{RIS}}$  increases, the attenuation of the target return from the reflection path becomes weaker due to longer propagation. Although the clutter strength is also weaker, the contributing clutter region is enlarged resulting in an overall decreasing trend of the SCR value. Based on the analysis above, a preliminary conclusion can be drawn that, from the radar perspective on target detection, shortening the target N-LoS propagation is advantageous to avoid a large clutter region.

### III. PROBLEM FORMULATION

Recall that the LFM waveform is simply used throughout the previous analysis on the clutter region issue. It raises a conjecture naturally that, beyond shortening the clutter region through

<sup>4</sup>It is worth pointing out that the distribution information of these undesired scatters can be estimated based on a cognitive paradigm, by combining the terrainmap data and the RCS clutter models [39], [40], [41], [42], [43].

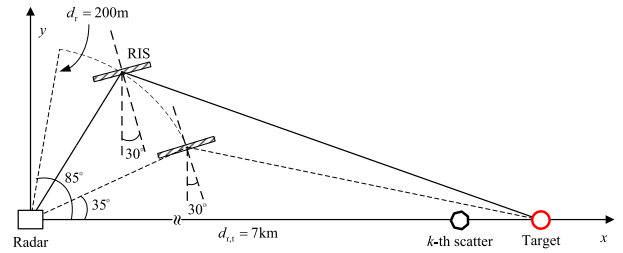


Fig. 4. Illustration on RIS position change.

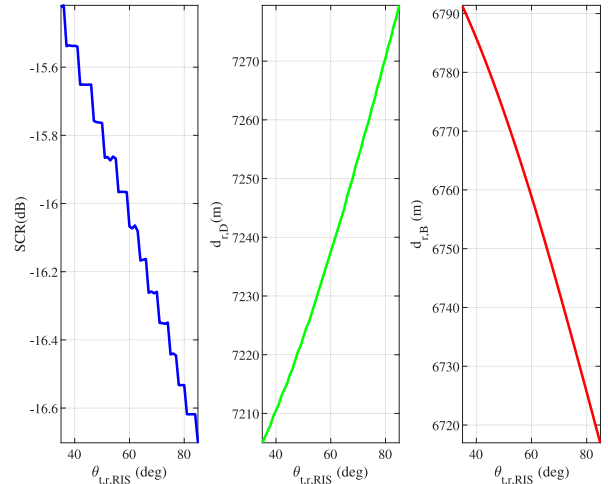


Fig. 5. SCR behavior versus  $\theta_{t,r,\text{RIS}}$ .

RIS placement, optimizing the radar waveform could also improve the target detection performance. In this section, we will formulate the detection performance enhancement problem for the RIS-aided radar system through the joint configuration of RIS phase, radar transmits waveform and receive filter. Based on the close relationship between target detection probability and system SINR under Gaussian background [41], [44], SINR is selected as the objective to optimize in this paper, where the N-LoS target return reflected by RIS is treated as critical usable information for performance enhancement. The SINR expression in this context is given as

$$\text{SINR}(\mathbf{w}, \mathbf{s}, \phi) = \frac{\mathbb{E} \left\{ |\mathbf{w}^\dagger \mathbf{y}_t|^2 \right\}}{\mathbb{E} \left\{ \left| \sum_{k=1}^K \mathbf{w}^\dagger \mathbf{y}_{c,k} \right|^2 \right\}} + \mathbf{w}^\dagger \mathbf{R}_n \mathbf{w}, \quad (13)$$

where  $\mathbf{w} \in \mathbb{C}^{r_{\text{data}}}$  denotes the filter vector. Note that  $\mathbb{E} \left\{ \left| \sum_{k=1}^K \mathbf{w}^\dagger \mathbf{y}_{c,k} \right|^2 \right\} = \sum_{k=1}^K \ddot{\sigma}_k^E \mathbf{w}^\dagger \mathbf{H}_{c,k}(\phi) \mathbf{s} \mathbf{s}^\dagger \mathbf{H}_{c,k}^\dagger(\phi) \mathbf{w}$ , we obtain the following exact SINR expression

$$\begin{aligned} \text{SINR}(\mathbf{w}, \mathbf{s}, \phi) &= \frac{\dot{\sigma}^E |\mathbf{w}^\dagger \mathbf{H}_t(\phi) \mathbf{s}|^2}{\mathbf{w}^\dagger \left( \sum_{k=1}^K \ddot{\sigma}_k^E \mathbf{H}_{c,k}(\phi) \mathbf{s} \mathbf{s}^\dagger \mathbf{H}_{c,k}^\dagger(\phi) + \mathbf{R}_n \right) \mathbf{w}}. \end{aligned} \quad (14)$$

Compared with the waveform design problem for traditional radar systems [41], [42], [45], the additional variable  $\phi$  is

involved in the SINR expression for the RIS-aided radar system. In this context, we consider the joint design of radar transmit waveform, receive filter and RIS phase shifts to improve the SINR given in (14), and formulate the joint optimization problem as

$$\mathcal{P} \begin{cases} \max_{\mathbf{w}, \mathbf{s}, \phi} \frac{\sigma^E |\mathbf{w}^\dagger \mathbf{H}_t(\phi) \mathbf{s}|^2}{\mathbf{w}^\dagger \left( \sum_{k=1}^K \ddot{\sigma}_k^E \mathbf{H}_{c,k}(\phi) \mathbf{s} \mathbf{s}^\dagger \mathbf{H}_{c,k}^\dagger(\phi) + \mathbf{R}_n \right) \mathbf{w}} \\ \text{s.t. } \mathbf{s} \in \Omega, \phi \in \Xi, \end{cases} \quad (15)$$

where  $\Omega$  and  $\Xi$  represent the admissible sets of radar waveform and RIS RCV, respectively. According to  $\mathcal{P}$ , the optimization requires prior knowledge about  $\{\ddot{\sigma}_k^E\}_{k=1}^K$  and  $\mathbf{R}_n$  in the operating environment, which is admissible once a cognitive scheme is assumed [43], [46].

In order to define the admissible sets of the problem (15), we force the following constraints:

- The transmitted waveform should possess constant envelope [39], i.e.,  $|s_l| = \sqrt{\frac{e_t}{L}}$ ,  $l = 1, 2, \dots, L$  where  $e_t$  is the total transmit energy.
- The resulting solution should be sufficiently close to some standard radar waveform possessing desirable properties in terms, e.g., of autocorrelation and range resolution, which implies forcing the *similarity constraint*  $\|\mathbf{s} - \mathbf{s}_{\text{ref}}\|_2^2 \leq \delta \cdot e_t$ , where  $\mathbf{s}_{\text{ref}} \in \mathbb{C}^L$  is the reference waveform and  $\delta$  is the parameter ruling the similarity [47], [48].
- To control the interference induced on spectrally adjacent systems, we limit the energy of the optimized waveform on the frequency bands of other licensed radiators [40], [41]. Suppose that there are  $Q$  frequency bands for as many licensed radiators with the  $q$ -th frequency band given as  $[f_1^q, f_2^q]$ . The energy of the waveform at  $q$ -th interval is calculated as  $\mathbf{s}^\dagger \mathbf{R}_q \mathbf{s}$ , where  $\mathbf{R}_q(m, n) = f_2^q - f_1^q$  for  $m = n$  and  $\mathbf{R}_q(m, n) = j \frac{e^{j2\pi f_1^q(m-n)} - e^{j2\pi f_2^q(m-n)}}{2\pi(m-n)}$  for  $m \neq n$ . Therefore, the total energy of the transmit waveform in the  $Q$  bands can be calculated as  $\sum_{q=1}^Q \beta_q \mathbf{s}^\dagger \mathbf{R}_q \mathbf{s} \leq e_{sc}$ , where  $e_{sc}$  gives the maximum permitting energy and  $\beta_q$  is weighting parameter for  $q$ -th band. For expression brevity, we reformulate the above inequality in matrix form, namely  $\mathbf{s}^\dagger \tilde{\mathbf{R}}_{\text{sum}} \mathbf{s} \leq e_{sc}$ , where  $\tilde{\mathbf{R}}_{\text{sum}} = \sum_{q=1}^Q \beta_q \mathbf{R}_q$ .

In conclusion, the set  $\Omega$  in (15) is defined as

$$\Omega = \left\{ \mathbf{s} \in \mathbb{C}^L \mid |s_l| = \sqrt{\frac{e_t}{L}}, l = 1, 2, \dots, L, \|\mathbf{s} - \mathbf{s}_{\text{ref}}\|_2^2 \leq \delta, \mathbf{s}^\dagger \tilde{\mathbf{R}}_{\text{sum}} \mathbf{s} \leq e_{sc} \right\}. \quad (16)$$

As to the constraints on the RIS phase shifts, we assume that each element of RIS is able to generate  $N_{\text{RCV}}$  available phase shifts uniformly distributed within  $[0, 2\pi]$  with interval  $\frac{2\pi}{N_{\text{RCV}}}$ . In other words, the phases of the RCV are assumed to lie in a

finite alphabet set, whereby the feasible set  $\Xi$  is composed of all available RCV and can be given as

$$\Xi = \{ \phi \in \mathbb{C}^N \mid |\phi_n| = 1, \varphi_n = \arg(\phi_n) \in \Phi, n = 1, 2, \dots, N \}, \quad (17)$$

where  $\Phi = \{0, \Delta\vartheta, \dots, (N_{\text{RCV}} - 1) \Delta\vartheta\}$  with  $\Delta\vartheta = \frac{2\pi}{N_{\text{RCV}}}$ .

Based on the analysis above, the joint design problem can be cast as

$$\mathcal{P} \begin{cases} \max_{\mathbf{w}, \mathbf{s}, \phi} \frac{\sigma^E |\mathbf{w}^\dagger \mathbf{H}_t(\phi) \mathbf{s}|^2}{\mathbf{w}^\dagger \left( \sum_{k=1}^K \ddot{\sigma}_k^E \mathbf{H}_{c,k}(\phi) \mathbf{s} \mathbf{s}^\dagger \mathbf{H}_{c,k}^\dagger(\phi) + \mathbf{R}_n \right) \mathbf{w}} \\ \text{s.t. } |s_l| = \sqrt{\frac{e_t}{L}}, l = 1, 2, \dots, L, \\ \|\mathbf{s} - \mathbf{s}_{\text{ref}}\|_2^2 \leq \delta \cdot e_t, \mathbf{s}^\dagger \tilde{\mathbf{R}}_{\text{sum}} \mathbf{s} \leq e_{sc}, \\ |\phi_n| = 1, \varphi_n = \arg(\phi_n) \in \Phi, n = 1, 2, \dots, N. \end{cases} \quad (18)$$

It is seen that  $\mathcal{P}$  is a non-convex optimization problem due to both the complicated objective (three variables are involved) and the non-convex constraints (especially the polyphase constraint for  $\phi$ ), which is NP-hard [49]. To this end, in the following section, an effective algorithm is developed based on the alternating optimization framework, which converts  $\mathcal{P}$  into more addressable subproblems.

#### IV. DEVELOPED ALGORITHM

In this section, an alternating optimization framework is devised to monotonically enhancing the SINR for the RIS-aided radar system with guaranteed convergence. To begin with, observing that  $\mathcal{P}$  is actually a generalized Rayleigh quotient w.r.t  $\mathbf{w}$ , we can easily obtain optimal solution to  $\mathcal{P}$  as  $\mathbf{w} = a \Psi^{-1}(\mathbf{s}, \phi) \mathbf{H}_t(\phi) \mathbf{s}$ , where  $a$  is an arbitrary non-zero scalar,  $\Psi(\mathbf{s}, \phi) = \sum_{k=1}^K \ddot{\sigma}_k^E \mathbf{H}_{c,k}(\phi) \mathbf{s} \mathbf{s}^\dagger \mathbf{H}_{c,k}^\dagger(\phi) + \mathbf{R}_n$ . Therefore, an equivalent form of  $\mathcal{P}$  can be obtained as

$$\tilde{\mathcal{P}} \begin{cases} \max_{\mathbf{s}, \phi} \mathbf{s}^\dagger \mathbf{H}_t^\dagger(\phi) \Psi^{-1}(\mathbf{s}, \phi) \mathbf{H}_t(\phi) \mathbf{s} \\ \text{s.t. } |s_l| = \sqrt{\frac{e_t}{L}}, l = 1, 2, \dots, L, \\ \|\mathbf{s} - \mathbf{s}_{\text{ref}}\|_2^2 \leq \delta \cdot e_t, \mathbf{s}^\dagger \tilde{\mathbf{R}}_{\text{sum}} \mathbf{s} \leq e_{sc}, \\ |\phi_n| = 1, \varphi_n = \arg(\phi_n) \in \Phi, n = 1, 2, \dots, N, \end{cases} \quad (19)$$

where  $\sigma^E$  has been omitted for simplicity since it is independent with the optimization process. However,  $\tilde{\mathcal{P}}$  is still hard to tackle directly. Observing the  $\tilde{\mathcal{P}}$  now is the optimization w.r.t  $\mathbf{s}$  and  $\phi$ , we propose to deal with  $\tilde{\mathcal{P}}$  by dividing it into two more tractable subproblems based on an alternating framework. Denote by the optimization objective of  $\tilde{\mathcal{P}}$  as  $f(\mathbf{s}, \phi)$ . Then, at  $i$ -th iteration, we start the optimization of radar waveform with fixed RIS RCV  $\phi^{(i-1)}$ , and seek for the admissible waveform  $\mathbf{s}^{(i)}$  maximizing  $f(\mathbf{s}^{(i)}, \phi^{(i-1)})$ ; after  $\mathbf{s}^{(i)}$  is obtained, we search for the RIS RCV which maximizes  $f(\mathbf{s}^{(i)}, \phi^{(i)})$ .

Mathematically, at  $i$ -th iteration, the above-mentioned two subproblems are cast as:

$$\tilde{\mathcal{P}}_s^{(i)} \begin{cases} \max_{\mathbf{s}} \mathbf{s}^\dagger \mathbf{H}_t^\dagger \left( \phi^{(i-1)} \right) \Psi^{-1} \left( \mathbf{s}, \phi^{(i-1)} \right) \mathbf{H}_t \left( \phi^{(i-1)} \right) \mathbf{s} \\ s.t. |s_l| = \sqrt{\frac{e_t}{L}}, l = 1, 2, \dots, L, \\ \|\mathbf{s} - \mathbf{s}_{\text{ref}}\|_2^2 \leq \delta \cdot e_t, \mathbf{s}^\dagger \tilde{\mathbf{R}}_{\text{sum}} \mathbf{s} \leq e_{sc}, \end{cases} \quad (20)$$

and

$$\tilde{\mathcal{P}}_\phi^{(i)} \begin{cases} \max_{\phi} \mathbf{s}^{(i)\dagger} \mathbf{H}_t^\dagger \left( \phi \right) \Psi^{-1} \left( \mathbf{s}^{(i)}, \phi \right) \mathbf{H}_t \left( \phi \right) \mathbf{s}^{(i)} \\ s.t. |\phi_n| = 1, \varphi_n = \arg(\phi_n) \in \Phi, n = 1, 2, \dots, N, \end{cases} \quad (21)$$

where  $(\mathbf{s}^{(i-1)}, \phi^{(i-1)})$  stands for the optimization result at the  $(i-1)$ -th iteration. Hence, the subsequent content mainly focuses on addressing  $\tilde{\mathcal{P}}_s^{(i)}$  and  $\tilde{\mathcal{P}}_\phi^{(i)}$  to perform the above-mentioned alternating optimization.

#### A. Solving $\tilde{\mathcal{P}}_s^{(i)}$

Note that  $\tilde{\mathcal{P}}_s^{(i)}$  is non-convex due to the complex objective function and non-convex waveform constant modulus restriction. The following proposition reveals that through solving a sequence of convex problems, a suboptimal solution to  $\tilde{\mathcal{P}}_s^{(i)}$  can be obtained with some property guarantees.

*Proposition 2:* The solution to  $\tilde{\mathcal{P}}_s^{(i)}$  can be obtained through solving a series of convex Quadratic Constraint Quadratic Programming (QCQP) problems  $\{\tilde{\mathcal{P}}_{s,(m)}\}_{m=1}^\infty$  to convergence, where  $\tilde{\mathcal{P}}_{s,(m)}$  is given as

$$\tilde{\mathcal{P}}_{s,(m)} \begin{cases} \max_{\mathbf{s}, \boldsymbol{\eta}} f_{\text{WAVE}}(\mathbf{s}; \mathbf{s}_{(m-1)}) - \varsigma \|\boldsymbol{\eta}\|_2 \\ s.t. |s_l| \leq \sqrt{\frac{e_t}{L}}, l = 1, 2, \dots, L, \\ 2\Re \{s_l^* s_{(m-1),l}\} - |s_{(m-1),l}|^2 \geq \frac{e_t}{L} - \eta_l, \\ l = 1, 2, \dots, L, \\ \|\mathbf{s} - \mathbf{s}_{\text{ref}}\|_2^2 \leq \delta \cdot e_t, \\ \mathbf{s}^\dagger \tilde{\mathbf{R}}_{\text{sum}} \mathbf{s} \leq e_{sc}, \\ \boldsymbol{\eta} \succeq 0, \boldsymbol{\eta}_{(m-1)} \succeq \boldsymbol{\eta}, \\ f_{\text{WAVE}}(\mathbf{s}; \mathbf{s}_{(m-1)}) \geq f(\mathbf{s}_{(m-1)}), \end{cases} \quad (22)$$

where  $\boldsymbol{\eta} \in \mathbb{C}^L$  is auxiliary variable,  $f_{\text{WAVE}}(\mathbf{s}; \mathbf{s}_{(m-1)}) = -\sum_{k=1}^K \ddot{\sigma}_k^E \mathbf{s}^\dagger \mathbf{H}_{c,k}^\dagger \mathbf{v} \mathbf{v}^\dagger \mathbf{H}_{c,k} \mathbf{s} + 2\Re \{ \mathbf{v}^\dagger \mathbf{H}_t \mathbf{s} \} - \mathbf{v}^\dagger \mathbf{R}_n \mathbf{v}$ ,  $\mathbf{v} = \Psi^{-1}(\mathbf{s}_{(m-1)}) \mathbf{H}_t \mathbf{s}_{(m-1)}$  with  $\mathbf{s}_{(m-1)}$  be the solution to  $(m-1)$ -th QCQP problem,  $\varsigma$  is a penalty parameter and  $\eta$  is a non-negative slack variable. Denote the waveform vector at convergence by  $\mathbf{s}^{(i)}$ , then  $\mathbf{s}^{(i)}$  is a KKT point of  $\tilde{\mathcal{P}}_s^{(i)}$ .

*Proof:* See Appendix B.  $\blacksquare$

Based on proposition 1, we can effectively obtain the solution to  $\tilde{\mathcal{P}}_s^{(i)}$  through solving a series of convex problems in polynomial time. The procedure is summarized in **Algorithm 1**.

*Remark:* The constraint  $f_{\text{WAVE}}(\mathbf{s}; \mathbf{s}_{(m-1)}) \geq f(\mathbf{s}_{(m-1)})$  is imposed to guarantee the monotonically increasing SINR property with iterations. It is worth pointing out that although

---

#### Algorithm 1 Procedure for solving $\tilde{\mathcal{P}}_s^{(i)}$

---

**Input:**  $\mathbf{s}^{(i-1)}, \phi^{(i-1)}, \{\ddot{\sigma}_k^E\}_{k=1}^K, \dot{\varphi}, \{\dot{\varphi}_n\}_{n=1}^N, \{\dot{\varphi}_k\}_{k=1}^K, \{\ddot{\varphi}_{k,n}\}_{k=1,n=1}^{K,N}, \{\dot{r}_n\}_{n=1}^N, \{\ddot{r}_k\}_{k=1}^K, \{\ddot{r}_{k,n}\}_{k=1,n=1}^{K,N}, \mathbf{R}_n$ .

**Output:**  $\mathbf{s}^{(i)}$ .

- 1: Set  $m = 1$ , let  $\mathbf{s}_{(m-1)} = \mathbf{s}^{(i-1)}$  and  $\varsigma = f_{\text{WAVE}}(\mathbf{s}^{(i-1)})$ .
  - 2: Compute  $\mathbf{H}_t, \{\mathbf{H}_{c,k}\}_{k=1}^K$ .
  - 3: **repeat**
  - 4: Calculate  $\mathbf{v}$  based on  $\mathbf{s}_{(m-1)}$ , and solve  $\tilde{\mathcal{P}}_{s,(m)}$  via interior point method to obtain  $\mathbf{s}_{(m)}$ .
  - 5:  $m \leftarrow m + 1$ .
  - 6: **until** Convergence
  - 7: **Output**  $\mathbf{s}^{(i)} = \mathbf{s}_{(m)}$ .
- 

the convergence of iteration can be still ensured without this constraint, the SINR performance at convergence has no theoretical guarantee.

#### B. Solving $\tilde{\mathcal{P}}_\phi^{(i)}$

This section mainly concentrate on addressing  $\tilde{\mathcal{P}}_\phi^{(i)}$ . To begin, notice that by defining

$$\begin{cases} \boldsymbol{\mu}_t = \dot{\alpha} e^{j\dot{\varphi}} \mathbf{J}_0 \mathbf{s}^{(i-1)} \\ \mathbf{M}_t = [\dot{\alpha}_1 e^{j\dot{\varphi}_1} \mathbf{J}_{\dot{r}_1} \mathbf{s}^{(i-1)}, \dots, \dot{\alpha}_N e^{j\dot{\varphi}_N} \mathbf{J}_{\dot{r}_N} \mathbf{s}^{(i-1)}] \end{cases} \quad (23)$$

we can simplify  $\mathbf{H}_t(\phi) \mathbf{s}^{(i-1)}$  into

$$\begin{aligned} \mathbf{H}_t(\phi) \mathbf{s}^{(i-1)} &= \left( \dot{\alpha} e^{j\dot{\varphi}} \mathbf{J}_0 + \sum_{n=1}^N \dot{\alpha}_n \phi_n e^{j\dot{\varphi}_n} \mathbf{J}_{\dot{r}_n} \right) \mathbf{s}^{(i-1)} \\ &= \boldsymbol{\mu}_t + \mathbf{M}_t \phi. \end{aligned} \quad (24)$$

Furthermore, let  $\tilde{\mathbf{M}}_t = [\mathbf{M}_t, \boldsymbol{\mu}_t]$ , and define a new variable  $\tilde{\phi} = (e^{j\varsigma} \phi^T, e^{j\varsigma})^T$ , we can further modify (24) into

$$\mathbf{H}_t(\phi) \mathbf{s}^{(i-1)} = e^{-j\varsigma} \tilde{\mathbf{M}}_t \tilde{\phi}. \quad (25)$$

Follow the similar definition, by defining  $\tilde{\mathbf{M}}_{c,k} = [\mathbf{M}_{c,k}, \boldsymbol{\mu}_{c,k}]$ , where

$$\begin{cases} \boldsymbol{\mu}_{c,k} = \ddot{\alpha}_k e^{j\dot{\varphi}_k} \mathbf{J}_{\dot{r}_k} \mathbf{s}^{(i-1)} \\ \mathbf{M}_{c,k} = [\ddot{\alpha}_{k,1} e^{j\dot{\varphi}_{k,1}} \mathbf{J}_{\dot{r}_{k,1}} \mathbf{s}^{(i-1)}, \dots, \ddot{\alpha}_{k,N} e^{j\dot{\varphi}_{k,N}} \mathbf{J}_{\dot{r}_{k,N}} \mathbf{s}^{(i-1)}] \end{cases} \quad (26)$$

we can re-express the matrix inversion item  $\mathbf{H}_{c,k}(\phi) \mathbf{s}$  in the optimization objective of  $\tilde{\mathcal{P}}_\phi^{(i)}$  as

$$\begin{aligned} \mathbf{H}_{c,k}(\phi) \mathbf{s}^{(i-1)} &= \boldsymbol{\mu}_{c,k} + \mathbf{M}_{c,k} \phi \\ &= e^{-j\varsigma} \tilde{\mathbf{M}}_{c,k} \tilde{\phi}. \end{aligned} \quad (27)$$

Accordingly, the feasible set for  $\tilde{\phi}$  can be cast as

$$\begin{aligned} \tilde{\Xi} &= \left\{ \tilde{\phi} \in \mathbb{C}^N \mid |\tilde{\phi}_n| = 1, \arg(\tilde{\phi}_{N+1}) \in \bar{\Phi}, \right. \\ &\quad \left. \tilde{\varphi}_n = \arg \left( \frac{\tilde{\phi}_n}{\tilde{\phi}_{N+1}} \right) \in \Phi, n = 1, 2, \dots, N \right\}, \end{aligned} \quad (28)$$



where the angle of  $\tilde{\phi}_{N+1}$  is constrained in  $\bar{\Phi}$  as limitation<sup>5</sup>.

Combining the transformations derived above, to obtain solution for  $\tilde{\mathcal{P}}_{\tilde{\phi}}^{(i)}$ , we can equivalently turn to address the following formulated problem

$$\mathcal{P}_{\tilde{\phi}} \begin{cases} \max_{\tilde{\phi}} \tilde{\phi}^\dagger \tilde{\mathbf{M}}_t^\dagger \Psi^{-1}(\tilde{\phi}) \tilde{\mathbf{M}}_t \tilde{\phi} \\ \text{s.t. } |\tilde{\phi}_n| = 1, \arg(\tilde{\phi}_{N+1}) \in \bar{\Phi}, \\ \tilde{\varphi}_n = \arg\left(\frac{\tilde{\phi}_n}{\tilde{\phi}_{N+1}}\right) \in \Phi, n = 1, 2, \dots, N, \end{cases} \quad (29)$$

where  $\Psi(\tilde{\phi}) = \sum_{k=1}^K \ddot{\sigma}_k^E \tilde{\mathbf{M}}_{c,k} \tilde{\phi} \tilde{\phi}^\dagger \tilde{\mathbf{M}}_{c,k}^\dagger + \mathbf{R}_n$ . Specifically, suppose  $\tilde{\phi}^*$  is a solution to  $\mathcal{P}_{\tilde{\phi}}$ , then it can be verified that the solution to the original problem  $\tilde{\mathcal{P}}_{\tilde{\phi}}^{(i)}$  can be constructed as  $\phi_n^{(i)} = \frac{\tilde{\phi}_n^*}{\tilde{\phi}_{N+1}^*}, n = 1, 2, \dots, N$ . Therefore, it is reasonable to investigate on solving  $\mathcal{P}_{\tilde{\phi}}$  to obtain solution to  $\tilde{\mathcal{P}}_{\tilde{\phi}}^{(i)}$ .

Following the same line of reasoning in Section IV-A, we can minorize the objective function of  $\mathcal{P}_{\tilde{\phi}}$  at  $m$ -th inner iteration as

$$f_{\text{RIS}}(\tilde{\phi}; \tilde{\phi}_{(m-1)}) = -\mathbf{g}^\dagger \Psi(\tilde{\phi}) \mathbf{g} + 2\Re\{\mathbf{g}^\dagger \tilde{\mathbf{M}}_t \tilde{\phi}\}, \quad (30)$$

where  $\mathbf{g} = \Psi^{-1}(\tilde{\phi}_{(m-1)}) \tilde{\mathbf{M}}_t \tilde{\phi}_{(m-1)}$ .

By substituting the exact expression of  $\Psi(\tilde{\phi})$  into  $f_{\text{RIS}}(\tilde{\phi}; \tilde{\phi}_{(m-1)})$ , it is easy to check that  $f_{\text{RIS}}(\tilde{\phi}; \tilde{\phi}_{(m-1)})$  is tantamount to the following quadratic formulation:

$$f_{\text{RIS}}(\tilde{\phi}; \tilde{\phi}_{(m-1)}) = -\tilde{\phi}^\dagger \left( \sum_{k=1}^K \ddot{\sigma}_k^E \tilde{\mathbf{M}}_{c,k}^\dagger \mathbf{g} \mathbf{g}^\dagger \tilde{\mathbf{M}}_{c,k} \right) \tilde{\phi} + 2\Re\{\mathbf{g}^\dagger \tilde{\mathbf{M}}_t \tilde{\phi}\} - \mathbf{g}^\dagger \mathbf{R}_n \mathbf{g}. \quad (31)$$

It is seen that (31) is already a convex quadratic function. Nevertheless, the non-convex polyphase constraints imposed on  $\tilde{\phi}$  make the resultant problem still very hard to tackle. In the following content, we will show that by further minorizing  $f_{\text{RIS}}(\tilde{\phi}; \tilde{\phi}_{(m-1)})$  into linear form, quasi-closed-form solution to resultant optimization problem can be given, even though the polyphase constraints on  $\tilde{\phi}$  are highly non-convex. To this end, the following lemma must be introduced.

*Lemma 1:* Let  $\mathbf{X}_1 \in \mathbb{C}^N$  be a Hermitian matrix, then  $\forall \bar{\mathbf{y}} \in \mathbb{C}^N$  the following inequality holds:

$$\mathbf{y}^\dagger \mathbf{X}_1 \mathbf{y} \leq \mathbf{y}^\dagger \mathbf{X}_2 \mathbf{y} + 2\Re\{\mathbf{y}^\dagger (\mathbf{X}_1 - \mathbf{X}_2) \bar{\mathbf{y}}\} + \bar{\mathbf{y}}^\dagger (\mathbf{X}_2 - \mathbf{X}_1) \bar{\mathbf{y}}, \quad (32)$$

where  $\mathbf{X}_2 \in \mathbb{C}^N$  is an arbitrary Hermitian matrix satisfying  $\mathbf{X}_2 \succeq \mathbf{X}_1$ .

For the detailed proof of lemma 1, readers can refer to [50], [51]. Following the lemma above, we can further minorize  $f_{\text{RIS}}(\tilde{\phi}; \tilde{\phi}_{(m-1)})$ . In detail, replace  $\mathbf{X}_1$  with  $\sum_{k=1}^K \ddot{\sigma}_k^E \tilde{\mathbf{M}}_{c,k}^\dagger \mathbf{g} \mathbf{g}^\dagger \tilde{\mathbf{M}}_{c,k}$  and let  $\mathbf{X}_2$  be a diagonal matrix with

<sup>5</sup>The choice of  $\tilde{\phi}_{N+1}$  is arbitrary since it is introduced as an auxiliary variable. It is worth highlighting that the selecting  $\Phi$  as the admissible region for angle of  $\tilde{\phi}_{N+1}$  will benefit us in obtaining quasi-closed-form solution for  $\varphi$ , as shown later in this section.

diagonal elements all being  $\text{Tr}\left(\sum_{k=1}^K \ddot{\sigma}_k^E \tilde{\mathbf{M}}_{c,k}^\dagger \mathbf{g} \mathbf{g}^\dagger \tilde{\mathbf{M}}_{c,k}\right)$ , it is seen that the precondition  $\mathbf{X}_2 \succeq \mathbf{X}_1$  has been satisfied. More importantly, since the modulus constraints hold for the RIS phase shifts, we have that  $\tilde{\phi}^\dagger \tilde{\phi} = N + 1$  and the quadratic term in the further minorizer can thereby be simplified as a constant  $(N + 1) \text{Tr}\left(\sum_{k=1}^K \ddot{\sigma}_k^E \tilde{\mathbf{M}}_{c,k}^\dagger \mathbf{g} \mathbf{g}^\dagger \tilde{\mathbf{M}}_{c,k}\right)$ . In short,  $f_{\text{RIS}}(\tilde{\phi}; \tilde{\phi}_{(m-1)})$  can now be tightly lower bounded by a linear function  $\tilde{f}_{\text{RIS}}(\tilde{\phi}; \tilde{\phi}_{(m-1)}) = 2\Re\{\tilde{\phi}^\dagger \tilde{\mathbf{g}}\} + \varpi$ , where

$$\begin{cases} \mathbf{G} = \sum_{k=1}^K \ddot{\sigma}_k^E \tilde{\mathbf{M}}_{c,k}^\dagger \mathbf{g} \mathbf{g}^\dagger \tilde{\mathbf{M}}_{c,k} \\ \quad - \text{Tr}\left(\sum_{k=1}^K \ddot{\sigma}_k^E \tilde{\mathbf{M}}_{c,k}^\dagger \mathbf{g} \mathbf{g}^\dagger \tilde{\mathbf{M}}_{c,k}\right) \mathbf{I}_{N+1} \\ \tilde{\mathbf{g}} = \tilde{\mathbf{M}}_t^\dagger \mathbf{g} - \mathbf{G} \tilde{\phi}_{(m-1)} \\ \varpi = -(N + 1) \text{Tr}\left(\sum_{k=1}^K \ddot{\sigma}_k^E \tilde{\mathbf{M}}_{c,k}^\dagger \mathbf{g} \mathbf{g}^\dagger \tilde{\mathbf{M}}_{c,k}\right) \\ \quad + \tilde{\phi}_{(m-1)}^\dagger \mathbf{G} \tilde{\phi}_{(m-1)} - \mathbf{g}^\dagger \mathbf{R}_n \mathbf{g} \end{cases}. \quad (33)$$

Combining the derivations above, we can further minorize  $f_{\text{RIS}}(\tilde{\phi}; \tilde{\phi}_{(m-1)})$  into the following linear function

$$\tilde{f}_{\text{RIS}}(\tilde{\phi}; \tilde{\phi}_{(m-1)}) = 2\Re\{\tilde{\phi}^\dagger \tilde{\mathbf{g}}\} + \varpi. \quad (34)$$

Therefore, it is clear that  $\tilde{f}_{\text{RIS}}(\tilde{\phi}; \tilde{\phi}_{(m-1)})$  is a tight minorizer to  $f_{\text{RIS}}(\tilde{\phi}; \tilde{\phi}_{(m-1)})$ . Ignoring the constant item, the optimization problem to deal with at  $m$ -th iteration can be formulated as

$$\tilde{\mathcal{P}}_{\tilde{\phi},(m)} \begin{cases} \max_{\tilde{\phi}} \Re\{\tilde{\phi}^\dagger \tilde{\mathbf{g}}\} \\ \text{s.t. } |\tilde{\phi}_n| = 1, \arg(\tilde{\phi}_{N+1}) \in \bar{\Phi}, \\ \tilde{\varphi}_n = \arg\left(\frac{\tilde{\phi}_n}{\tilde{\phi}_{N+1}}\right) \in \Phi, n = 1, 2, \dots, N. \end{cases} \quad (35)$$

Though the polyphase constraints on  $\tilde{\phi}$  are highly non-convex, it will be shown that quasi-closed-form solution to the resultant optimization can be given, which is concluded as the proposition given below.

*Proposition 3:* When the feasible set of  $\arg(\tilde{\phi}_{N+1})$  is chosen as  $\bar{\Phi}$ , i.e.  $\bar{\Phi} = \Phi$ , the constraint set in  $\tilde{\mathcal{P}}_{\tilde{\phi},(m)}$ , namely  $\bar{\Xi}$ , can be equivalently cast as

$$\bar{\Xi}' = \{\tilde{\phi} \in \mathbb{C}^N \mid |\tilde{\phi}_n| = 1, \tilde{\varphi}_n = \arg(\tilde{\phi}_n) \in \Phi, n = 1, 2, \dots, N + 1\}, \quad (36)$$

In this context,  $\tilde{\mathcal{P}}_{\tilde{\phi},(m)}$  is equal to the following problem

$$\begin{cases} \max_{\tilde{\phi}} \Re\{\tilde{\phi}^\dagger \tilde{\mathbf{g}}\} \\ \text{s.t. } |\tilde{\phi}_n| = 1, \arg(\tilde{\phi}_n) \in \Phi, \\ n = 1, 2, \dots, N + 1. \end{cases} \quad (37)$$

**Algorithm 2** Procedure for solving  $\tilde{\mathcal{P}}_\phi^{(i)}$ 

**Input:**  $\mathbf{s}^{(i)}$ ,  $\phi^{(i-1)}$ ,  $\{\ddot{\sigma}_k^E\}_{k=1}^K$ ,  $\dot{\phi}$ ,  $\{\dot{\varphi}_n\}_{n=1}^N$ ,  $\{\ddot{\varphi}_k\}_{k=1}^K$ ,  $\{\ddot{\varphi}_{k,n}\}_{k=1,n=1}^{K,N}$ ,  $\{\dot{r}_n\}_{n=1}^N$ ,  $\{\ddot{r}_k\}_{k=1}^K$ ,  $\{\ddot{r}_{k,n}\}_{k=1,n=1}^{K,N}$ ,  $\mathbf{R}_n$ .

**Output:**  $\phi^{(i)}$ .

- 1: Set  $m = 1$ , and let  $\phi_{(m-1)} = \phi^{(i-1)}$ .
- 2: Compute  $\{\tilde{\mathbf{M}}_{c,k}\}_{k=1}^K$ ,  $\tilde{\mathbf{M}}_t$ .
- 3: **repeat**
- 4: Calculate  $\tilde{\mathbf{g}}$  and  $\mathbf{h}$  based on  $\phi_{(m-1)}$ .
- 5: Update the RCV via  $\phi_{(m),n} = \frac{\phi_{(m),n}}{\phi_{(m),N+1}}$ ,  $n = 1, 2, \dots, N$   
where  $\tilde{\phi}_{(m)} = e^{j\mathbf{h}\Delta\vartheta}$ .
- 6:  $m \leftarrow m + 1$ .
- 7: **until** Convergence
- 8: **Output**  $\phi^{(i)} = \phi_{(m)}$ .

*Proof:* See Appendix C. ■

Based on lemma 1, it is equivalent to deal with (37) when we set  $\tilde{\Phi} = \Phi$ . In fact, a closer inspection of (37) reveals that it has quasi-closed-form solution given by  $\tilde{\phi} = e^{j\mathbf{h}\Delta\vartheta}$ , where  $\mathbf{h} = [h_1, h_2, \dots, h_{N+1}]^T \in \mathbb{R}^{N+1}$  with  $h_n = \arg \min_{h=0,1,\dots,N_{\text{RCV}}-1} |h\Delta\vartheta - \arg(\tilde{g}_n)|$ . To conclude, the optimization process for solving  $\tilde{\mathcal{P}}_\phi^{(i)}$  has been summarized in **Algorithm 2**.

### C. Initialization

The trigger of developed alternating algorithm requires an initial pair of waveform and RCV. Thus, it is essential to devise a suitable procedure to obtain a feasible waveform and RCV as initialization. To this end, the initial RIS RCV can be directly generated by randomly choosing some phase shifts from  $\Xi$ . The start waveform can be obtained by addressing

$$\begin{cases} \min_{\mathbf{s}} \mathbf{s}^\dagger \tilde{\mathbf{R}}_{\text{sum}} \mathbf{s} \\ \text{s.t. } |s_l| = \sqrt{\frac{e_t}{L}}, l = 1, 2, \dots, L, \\ \|\mathbf{s} - \mathbf{s}_{\text{ref}}\|_2^2 \leq \delta \cdot e_t. \end{cases} \quad (39)$$

It can be seen that (39) can be effectively solved via similar procedure utilized for solving  $\tilde{\mathcal{P}}_s^{(i)}$ . It is necessary to highlight that dealing with (39) also provide a way to check the feasibility of problem  $\mathcal{P}$ . Denote by the optimal value of (39) as  $e_{\text{sc}}^*$ , then  $\mathcal{P}$  is feasible only when  $e_{\text{sc}} \geq e_{\text{sc}}^*$ .

### D. Convergence and Complexity Analysis

In general, the convergence of the proposed algorithm is guaranteed by the alternating optimization scheme. Specifically, it follows that

$$f(\mathbf{s}^{(i-1)}, \phi^{(i-1)}) \leq f(\mathbf{s}^{(i-1)}, \phi^{(i)}) \leq f(\mathbf{s}^{(i)}, \phi^{(i)}). \quad (40)$$

As the index  $i$  increases,  $f(\mathbf{s}^{(i)}, \phi^{(i)})$  is monotonically improving. At the same time, due to the finite energy of waveform

**Algorithm 3** The alternating optimization based framework for solving  $\mathcal{P}$ 

**Input:**  $\{\ddot{\sigma}_k^E\}_{k=1}^K$ ,  $\dot{\phi}$ ,  $\{\dot{\varphi}_n\}_{n=1}^N$ ,  $\{\ddot{\varphi}_k\}_{k=1}^K$ ,  $\{\ddot{\varphi}_{k,n}\}_{k=1,n=1}^{K,N}$ ,  $\{\dot{r}_n\}_{n=1}^N$ ,  $\{\ddot{r}_k\}_{k=1}^K$ ,  $\{\ddot{r}_{k,n}\}_{k=1,n=1}^{K,N}$ ,  $\mathbf{R}_n$ .

**Output:** Optimized receive filter, transmit waveform and RCV pair  $(\mathbf{w}^*, \mathbf{s}^*, \phi^*)$ .

- 1: Set  $i = 1$ , initialize  $\mathbf{s}^{(0)}$  and  $\phi^{(0)}$ .
- 2: Call **Algorithm 1** to address  $\tilde{\mathcal{P}}_s^{(i)}$ , where input includes  $\mathbf{s}^{(i-1)}$ ,  $\phi^{(i-1)}$  and output is the waveform vector  $\mathbf{s}^{(i)}$ .
- 3: Call **Algorithm 2** to address  $\tilde{\mathcal{P}}_\phi^{(i)}$ , where input includes  $\mathbf{s}^{(i)}$ ,  $\phi^{(i-1)}$  and output is the RCV  $\phi^{(i)}$ .
- 4: **if** Converges **then**
- 5:   Cease the algorithm.
- 6: **else**
- 7:    $i \leftarrow i + 1$  and go to step 2.
- 8: **end if**
- 9: Output  $\mathbf{s}^* = \mathbf{s}^{(i)}$ ,  $\phi^* = \phi^{(i)}$  and calculate the filter as

$$\mathbf{w}^* = \alpha \Psi^{-1}(\mathbf{s}^*, \phi^*) \mathbf{H}_t (\phi^*) \mathbf{s}^*. \quad (38)$$

and RCV,  $f(\mathbf{s}^{(i)}, \phi^{(i)})$  is upper bounded. Thus, the convergence is ensured.

The main complexity of the devised **Algorithm 3** is linear with the number of iterations. In each iteration, **Algorithm 1** and **2** are applied to solve  $\tilde{\mathcal{P}}_s^{(i)}$  and  $\tilde{\mathcal{P}}_\phi^{(i)}$ , respectively. In terms of **Algorithm 1**, its complexity results from solving a series of formulated QCQP problems, where each optimization can be completed via interior point method in polynomial time with a computational cost of  $\mathcal{O}(L^3)$  [52]. Note that compared with the solving process of  $\tilde{\mathcal{P}}_s^{(i)}$ , quasi-closed-form solution is given for **Algorithm 2** at each iteration. Such fact reduces the calculation burden of **Algorithm 2** at each iteration but may lead to larger iteration number since the minorization is linear and thereby looser. At each iteration, the computational cost mainly come from the calculation of  $\tilde{\mathbf{g}}$  and  $\mathbf{h}$  which is about  $\mathcal{O}((N+1)^2)$ .

## V. SIMULATION RESULTS AND PERFORMANCE ANALYSIS

This section use a series of simulation experiments to demonstrate the effectiveness of the considered joint design on enhancing target detectability of the RIS-aided radar, in which the impact of system parameters and their interplay are also investigated.

The radar operates at the center frequency 3 GHz with 25 MHz bandwidth and 1.28  $\mu\text{s}$  pulse length (leading to  $N = 32$ ) and the transmit energy is set to be  $e_t = 0.01$ . The radar beam gains towards the target and RIS elements are set all identical as  $G_t = G_{\text{RIS},n} = 1$ ,  $n = 1, 2, \dots, N$ . Unless otherwise stated, we employ the scenario configuration shown as Fig. 6 and the geometry parameters utilized for simulation are listed in Table II. The target RCS is chosen as 0dBm. Considering that the undesired scatters are distributed along target direction and with identical RCS -20dBm. A LFM signal of the same duration



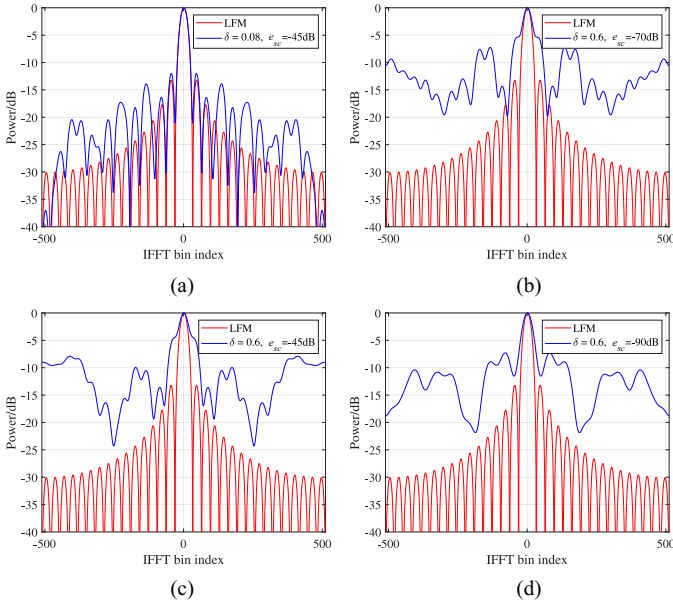


Fig. 9. Pulse compression properties of the waveform optimized by the proposed algorithm. (a)  $N = 64$ ,  $\delta = 0.08$ ,  $e_{sc} = -45\text{dB}$ , (b)  $N = 64$ ,  $\delta = 0.6$ ,  $e_{sc} = -70\text{dB}$ , (c)  $N = 64$ ,  $\delta = 0.6$ ,  $e_{sc} = -45\text{dB}$ , (d)  $N = 64$ ,  $\delta = 0.6$ ,  $e_{sc} = -90\text{dB}$ .

where  $\tilde{\mathbf{w}} \in \mathbb{C}^L$  and  $\tilde{\mathbf{s}} \in \mathbb{C}^L$  are the filter and transmit waveform,  $\tilde{\mathbf{J}}_r \in \mathbb{C}^{L \times L}$  and  $\mathbf{R}'_n \in \mathbb{C}^{L \times L}$  are the according shifting matrix and interference covariance matrix matching the size. It is obvious from the figure that the detection probability exhibits increasing behavior with larger RIS size and looser waveform constraints. Compared with conventional scheme, the RIS-aided radar system achieves significant detection performance improvement. Specifically, when  $\delta = 0.6$ , about 10dBsm stronger target RCS is required to attain the same detection performance as the radar system aided by an 128-element RIS.

### B. Radar Waveform and RIS Beampattern Characteristics

We next check the properties of the radar waveform and RIS RCV optimized by the proposed algorithm. Fig. 9 and Fig. 10 show the pulse compression and spectral characteristics of several optimized radar waveform sets, where  $N_{\text{RCV}} = 8$ . Looking over the figures unveils that restricted by the spectral constraint, the spectrum of optimized waveforms all form obvious concavities within the interval  $[0.3, 0.32]$  and  $[0.6, 0.62]$ . From Fig. 10(b), 10(e), and 10(f), it can be seen that under the same  $\delta$ , as the restriction on the ESD in the above bands is strengthened, deeper null is formed. Fig. 9 reveals that as  $\delta$  increases, the pulse compression characteristics of the optimized waveform become sharper and tend to approach that of the reference LFM signal. On the contrary, when  $\delta = 0.6$ , the sidelobe level of the waveform after matched filtering is high which leads to poor range resolution. In addition, from Fig. 10(a), 10(b), and 10(c), it can be seen that under the same spectral compatibility constraint, as tighter similarity is ruled, the overall spectrum of the optimized waveform becomes flatter and tends to approach the spectral characteristics of the reference LFM signal. To provide deeper insights into the interaction within

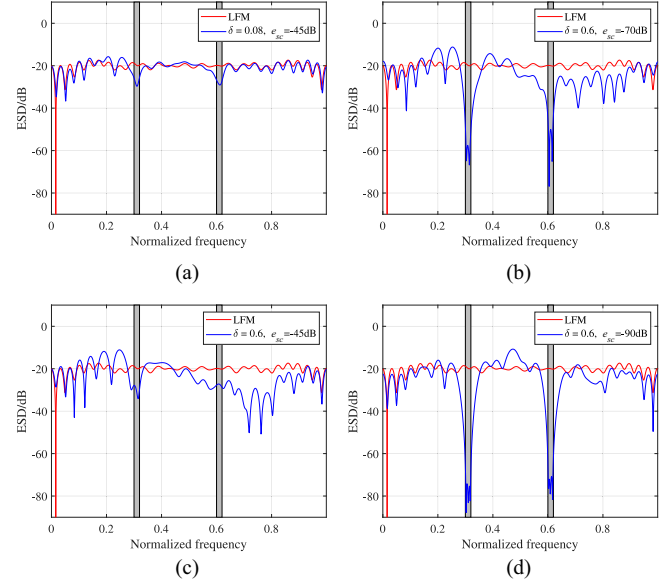


Fig. 10. ESD of the waveform optimized by the proposed algorithm versus normalized frequency. (a)  $N = 64$ ,  $\delta = 0.08$ ,  $e_{sc} = -45\text{dB}$ , (b)  $N = 64$ ,  $\delta = 0.6$ ,  $e_{sc} = -70\text{dB}$ , (c)  $N = 64$ ,  $\delta = 0.6$ ,  $e_{sc} = -45\text{dB}$ , (d)  $N = 64$ ,  $\delta = 0.6$ ,  $e_{sc} = -90\text{dB}$ .

the RIS-aided system, we subsequently analyze the RIS beampattern. Specifically, the beampattern of RIS with RCV  $\phi$  is calculated via

$$P_{\text{RIS}}(\theta) = |\mathbf{w}_{\text{RISBP}}^\dagger \mathbf{a}(\theta)|^2, \quad (44)$$

where  $\mathbf{w}_{\text{RISBP}} = \phi \odot \mathbf{b}$  with  $\mathbf{b} = [e^{-j2\pi \frac{d_r,1}{\lambda}}, e^{-j2\pi \frac{d_r,2}{\lambda}}, \dots, e^{-j2\pi \frac{d_r,N}{\lambda}}]^T \in \mathbb{C}^N$ , and  $\mathbf{a}(\theta) = [1, e^{j2\pi \frac{d_{\text{RIS}} \sin \theta}{\lambda}}, \dots, e^{j2\pi \frac{(N-1)d_{\text{RIS}} \sin \theta}{\lambda}}]^T \in \mathbb{C}^N$ . With the relative position the same as Fig. 6, two RIS spacing configurations are employed, where the inclination w.r.t the x-axis are  $20^\circ$  and  $30^\circ$  (leading to  $\theta_t^{\text{RIS}} = -59.9^\circ$  and  $\theta_t^{\text{RIS}} = -69.9^\circ$ ), respectively. As can be observed from Fig. 11, the main beam points towards the target direction at all cases. A comparison between Fig. 11(a) and 11(b) indicates that sharper mainlobe and lower sidelobe can be obtained through the usage of larger RIS. Moreover, the beampattern in Fig. 11(c) and 11(d) highlight the benefit of employing RIS with ability to generate more available phase shifts, since the sidelobe in Fig. 11(d) is significantly lower than that in Fig. 11(c) which leads to suppressed clutter energy and enhanced SINR as the result in Fig. 7 depicts. Based on the above analysis, a preliminary conclusion can be drawn that the main role RIS play in the system is to align the target echo and null the clutter through spatial beamforming<sup>6</sup>.

### C. Impact of the RIS Size and Placement

We now investigate on SINR of the RIS-aided radar system with different RIS sizes. In this example, the center position and placement direction of RIS remain the same as before. The other parameters are set as  $\delta = 0.6$ ,  $e_{sc} = -45\text{dB}$  and  $N_{\text{RCV}} = 8$ . To shed light on impact of range gate shift over RIS-aided radar

<sup>6</sup>If the far-field assumption between RIS and target no longer hold, a range-dependent two dimension beampattern should be investigated instead.



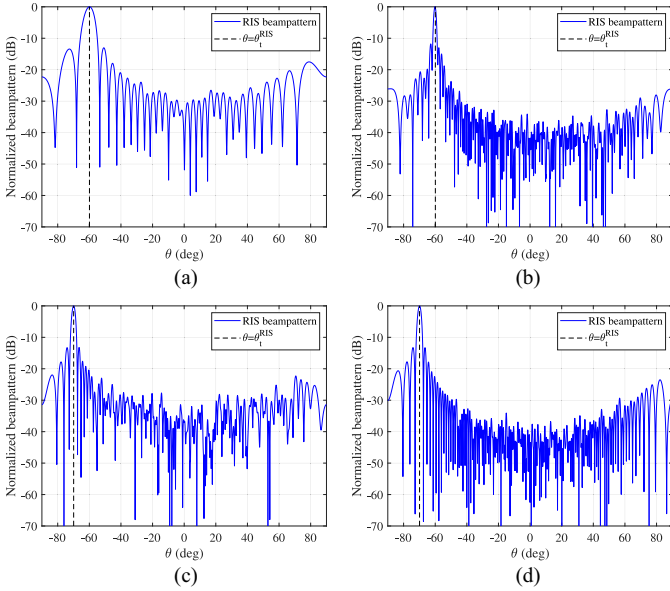


Fig. 11. RIS beampattern. (a)  $N = 32$ ,  $\theta_t^{\text{RIS}} = -59.9^\circ$ ,  $N_{\text{RCV}} = 32$ , (b)  $N = 128$ ,  $\theta_t^{\text{RIS}} = -59.9^\circ$ ,  $N_{\text{RCV}} = 32$ , (c)  $N = 128$ ,  $\theta_t^{\text{RIS}} = -69.9^\circ$ ,  $N_{\text{RCV}} = 8$ , (d)  $N = 128$ ,  $\theta_t^{\text{RIS}} = -69.9^\circ$ ,  $N_{\text{RCV}} = 32$ .

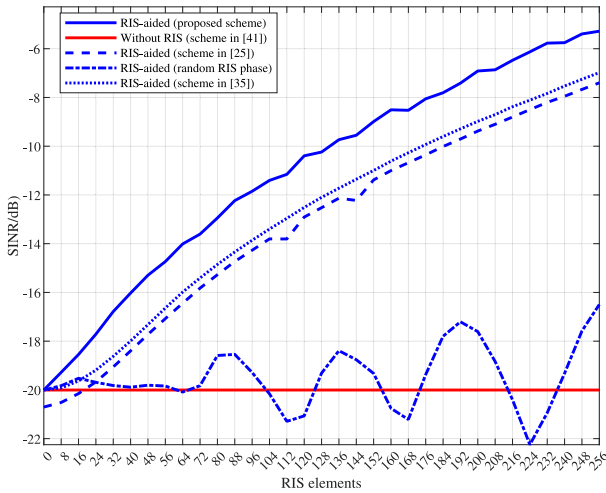


Fig. 12. SINR versus RIS elements. The geometry configuration is set as described in Fig. 6.  $\delta = 0.6$ ,  $e_{\text{sc}} = -45\text{dB}$ ,  $N_{\text{RCV}} = 8$ .

system, we verify the performance of our scheme in comparison with that in [35], where the range gate shifts caused by N-LoS propagation are ignored at the design stage. Moreover, for the elaboration on the importance of radar waveform and RIS RCV optimization process, we add another two RIS-aided schemes. In the former scheme fixed waveform and adjusted RIS RCV are utilized, as applied in [25]. In the latter scheme the waveform is optimized but random given RCV are utilized, denoted as ‘RIS-aided (random RIS phase)’. The curves depicted in Fig. 12 clearly emphasize the benefit of larger RIS size on providing distinct SINR gain. In particular, when the radar is aided by a 128-element RIS, the maximum SINR gain over the no-RIS scheme reaches about 10dB. The results also stressed the

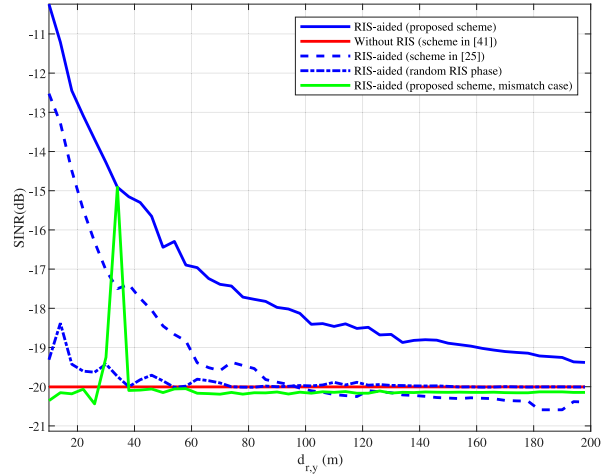


Fig. 13. SINR versus  $d_{r,y}$ .  $N = 128$ ,  $\delta = 0.6$ ,  $e_{\text{sc}} = -45\text{dB}$ ,  $N_{\text{RCV}} = 8$ .

superiority of our established model since it is observed that the neglect of range gate shift at the design stage has clearly lead to SINR losses. A closer inspect into the results reveals the dependence of system SINR on the transmit waveform. By transmitting tailored waveform instead of LFM signal, the RIS-aided radar system achieve more than 2dB SINR improvement when RIS size is larger than 16. In comparison to that, the choice of RIS RCV appears further crucial to system SINR, as the curve corresponding to random  $\phi$  indicates. Note that in some cases, the performance of RIS-aided radar with random  $\phi$  is even worse than the conventional scheme where no RIS is employed. In other words, the deployment of RIS without suitable configuration of its phase shifts can be even counter-productive. Indeed, the deployment of RIS can enhance SINR with adjusted RCV. However, mutual cancellation among the target returns may also be brought with inappropriate RCV and the original function of radar system can be devastated thereby.

The next example examines the impact of RIS placement on the SINR of RIS-aided radar system. In particular, with radar and target kept the same position as before and the placement direction of RIS unchanged as drawn in Fig. 6, move the 128-element RIS along the y-axis. Changing  $d_{r,y}$  from 10m to 200m, the SINR behavior is examined with  $\delta = 0.6$ ,  $e_{\text{sc}} = -45\text{dB}$  and  $N_{\text{RCV}} = 8$ . To verify the robustness of the RIS-aided system over RIS position, a mismatched scheme is added. That is, optimize a set of radar waveform and RIS RCV under the assumption that  $d_{r,y} = 34\text{m}$ , and calculate the according SINR of the RIS-aided system at various actual RIS positions. Fig. 13 stresses the advantage of close RIS deployment to radar, since higher SINR gain can be obtained. This is consistent with intuitive understanding. When the distance between radar and RIS is close enough, RIS-aided radar can be regarded as a multiple receive array system to some extent. As RIS is deployed far from radar, the SINR improvement compared to conventional radar system degrades. From the figure, it can be observed that the knowledge accuracy on the RIS position is significant. Specifically, the radar waveform and RIS RCV designed for  $d_{r,y} = 34\text{m}$  can achieve pleasant performance in matched RIS

position, but the SINR loss can be unaffordable in mismatched cases. Moreover, a obvious SINR degradation of the RIS-aided scheme with random  $\phi$  compared with the RIS-aided scheme is noticed, which stresses again the importance of RCV optimization procedure on system SINR.

## VI. CONCLUSION

This paper aims to enhance target detection performance under clutter background by deploying RIS in the scene and capitalizing on both the DoF at the radar and RIS. Compared with the existing works, the developed signal model considers the impact of the RIS's presence on the returns based on strict geometry and propagation rules, especially the range gate shifts brought by N-LoS propagation, which enhances the applicability of our model to account for more general cases. At the problem formulation stage, multiple waveform hallmarks and practical RIS hardware limitation are imposed in the formulated joint design, which makes the considered design more practical and represents the main innovation of this paper from the view of problem formulation. At the analysis stage, insights of the interplay among radar, RIS and target, in particular, impact of system parameters and the role RIS play in the system are given. Future research directions include extending this work to multiple RIS deployment scenarios and exploring RIS position optimization, given its impact on RIS-aided radar system performance as indicated in [53], [54].

## APPENDIX A

### PROOF OF PROPOSITION 1

For arbitrary point  $B'$  in the scene, if its N-LoS return (from the  $n$ -th element) can just separate with the target return at the head, the following condition holds

$$(d_{r,B'} + d_{B',n} + d_{r,n}) \frac{f_s}{c} = \left\lceil 2d_{r,t} \frac{f_s}{c} \right\rceil - L, \quad (45)$$

where  $d_{r,B'}$  and  $d_{B',n}$  stands for the physical distance between the radar and  $B'$ ,  $B'$  and  $n$ -th element of RIS, respectively.

According to (45), we have that

$$d_{B',n}^2 = \left( \left\lceil 2d_{r,t} \frac{f_s}{c} \right\rceil \frac{c}{f_s} - L \frac{c}{f_s} - d_{r,B'} - d_{r,n} \right)^2. \quad (46)$$

On the other hand, as shown in Fig. 14, when the angle formed by  $B'$ , radar and target is  $\theta$ , the cosine theorem indicates that  $d_{B',n}^2 = d_{r,n}^2 + d_{r,B'}^2 - 2d_{r,n}d_{r,B'} \cos \dot{\theta}_n$ , where  $\dot{\theta}_n$  is the angle formed by radar- $B'$  and radar- $n$ -th element of RIS.

Note that  $\dot{\theta}_n = \dot{\theta}_n - \theta$ , where  $\dot{\theta}_n$  is the angle formed by radar-target and radar- $n$ -th element of RIS. Hence, through some basic mathematical manipulations, one can easily derive the expression of  $d_{r,B'}$  as

$$d_{r,B'} = \frac{\left( 2d_{r,n} - \left\lceil 2d_{r,t} \frac{f_s}{c} \right\rceil \frac{c}{f_s} + L \frac{c}{f_s} \right) \left( \left\lceil 2d_{r,t} \frac{f_s}{c} \right\rceil \frac{c}{f_s} - L \frac{c}{f_s} \right)}{2 \left( d_{r,n} \cos(\dot{\theta}_n - \theta) + d_{r,n} - \left\lceil 2d_{r,t} \frac{f_s}{c} \right\rceil \frac{c}{f_s} + L \frac{c}{f_s} \right)}. \quad (47)$$

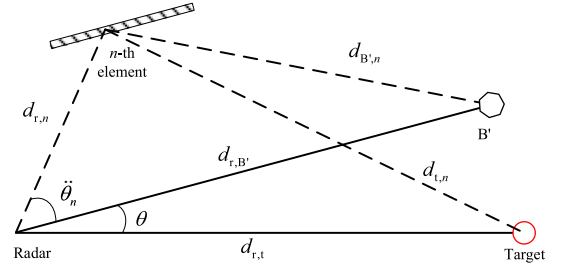


Fig. 14. Illustration of the geometry relationships.

At particular angle  $\theta$ , there is a one-to-one correspondence between  $d_{r,B'}$  and  $n$ . Denote by  $B$  and  $D$  the lower and upper boundaries of the clutter region in this direction<sup>7</sup>. Moreover, since the sought point  $B$  is the head border (close to radar) of clutter region for identification of return overlap, denote the  $n$  corresponds to  $d_{r,B}$  by  $n_B$ ,  $n_B$  meets the condition  $n_B = \arg \max_n \{d_{B',n} + d_{r,n}\}$  and relationship between  $d_{B',n}$  and  $d_{r,B'}$  can be reflected as  $d_{B',n}^2 = d_{r,n}^2 + d_{r,B'}^2 - 2d_{r,n}d_{r,B'} \cos(\dot{\theta}_n - \theta)$ . Therefore, at any direction  $\theta$ ,  $d_{r,B}$  can be computed through finding the  $n_B$  that maximizes  $d_{B',n} + d_{r,n}$  and substituting  $n$  with  $n_B$  in (47).

Resorting to the similar line of reasoning, we have that if  $D$  is the end border (far to radar) of the clutter region in the direction  $\theta$ , then its LoS return just overlaps with the target return which indicates the following relationship

$$\left\lceil (d_{r,t} + d_{t,n_D} + d_{r,n_D}) \frac{f_s}{c} \right\rceil = 2d_{r,D} \frac{f_s}{c} - (L - 1), \quad (48)$$

where  $n_D = \arg \max_n \{d_{t,n} + d_{r,n}\}$ . Therefore, one can directly get

$$d_{r,D} = \frac{\left\lceil (d_{r,t} + d_{t,n_D} + d_{r,n_D}) \frac{f_s}{c} \right\rceil \frac{c}{f_s} + (L - 1) \frac{c}{f_s}}{2}. \quad (49)$$

Combining (47), (49) and the analysis above, we can give the clutter region boundaries of RIS-aided radar as

$$\begin{cases} d_{r,B} = \frac{2d_{r,n_B} \frac{f_s}{c} - \left\lceil 2d_{r,t} \frac{f_s}{c} \right\rceil + L}{\left( \frac{d_{r,n_B} \cos(\dot{\theta}_{n_B} - \theta) + d_{r,n_B}}{\left\lceil 2d_{r,t} \frac{f_s}{c} \right\rceil \frac{c}{f_s} - L \frac{c}{f_s}} - 1 \right)} \frac{c}{2f_s} \\ d_{r,D} = \left( L - 1 + \left\lceil (d_{r,t} + d_{t,n_D} + d_{r,n_D}) \frac{f_s}{c} \right\rceil \right) \frac{c}{2f_s} \end{cases}, \quad (50)$$

where

$$\begin{cases} n_B = \arg \max_n \{d_{B',n} + d_{r,n}\} \\ n_D = \arg \max_n \{d_{t,n} + d_{r,n}\} \end{cases}. \quad (51)$$

<sup>7</sup>Here the ends of the clutter region means that the return of any point within  $BD$  will overlap with the target return while these points closer to radar than  $B$  and points farther to radar than  $D$  to radar have no contribution to the target return.

## APPENDIX B

## PROOF OF PROPOSITION 2

To begin with, it is necessary to highlight that for matrix  $\forall \mathbf{X} \succeq 0$ , the quadratic form  $\mathbf{y}^\dagger \mathbf{X}^{-1} \mathbf{y}$  is actually convex w.r.t  $(\mathbf{y}, \mathbf{X})$  [49]. Such result is easy to verify resorting to its Schur complement form. In light of the convexity of  $\mathbf{y}^\dagger \mathbf{X}^{-1} \mathbf{y}$ , we apply the first-order condition to obtain the following inequality

$$\begin{aligned} \mathbf{y}^\dagger \mathbf{X}^{-1} \mathbf{y} &\geq \bar{\mathbf{y}}^\dagger \bar{\mathbf{X}}^{-1} \bar{\mathbf{y}} + 2\Re \left\{ \bar{\mathbf{y}}^\dagger \bar{\mathbf{X}}^{-1} (\mathbf{y} - \bar{\mathbf{y}}) \right\} \\ &\quad - (\bar{\mathbf{X}}^{-1} \bar{\mathbf{y}})^\dagger (\mathbf{X} - \bar{\mathbf{X}}) (\bar{\mathbf{X}}^{-1} \bar{\mathbf{y}}) \\ &= -\bar{\mathbf{y}}^\dagger \bar{\mathbf{X}}^{-1} \mathbf{X} \bar{\mathbf{X}}^{-1} \bar{\mathbf{y}} + 2\Re \left\{ \bar{\mathbf{y}}^\dagger \bar{\mathbf{X}}^{-1} \mathbf{y} \right\}. \end{aligned} \quad (52)$$

It is seen that the right side of (52) provides a linear approximation to  $\mathbf{y}^\dagger \mathbf{X}^{-1} \mathbf{y}$  at point  $(\bar{\mathbf{y}}, \bar{\mathbf{X}})$ . Enlightened by the above result, we can obtain a minorizer to  $f(\mathbf{s})$ <sup>8</sup> as

$$f_{\text{WAVE}}(\mathbf{s}; \mathbf{s}_{(m-1)}) = -\mathbf{v}^\dagger \Psi(\mathbf{s}) \mathbf{v} + 2\Re \left\{ \mathbf{v}^\dagger \mathbf{H}_t \mathbf{s} \right\}, \quad (53)$$

where  $\mathbf{v} = \Psi^{-1}(\mathbf{s}_{(m-1)}) \mathbf{H}_t \mathbf{s}_{(m-1)}$  with  $\mathbf{s}_{(m-1)}$  be the optimized waveform at  $(m-1)$ -th inner iteration.

Note that  $\Psi(\mathbf{s}) = \sum_{k=1}^K \ddot{\sigma}_k^E \mathbf{H}_{c,k} \mathbf{s} \mathbf{s}^\dagger \mathbf{H}_{c,k}^\dagger + \mathbf{R}_n$ , we can reformulate  $f_{\text{WAVE}}(\mathbf{s}; \mathbf{s}_{(m-1)})$  into

$$\begin{aligned} f_{\text{WAVE}}(\mathbf{s}; \mathbf{s}_{(m-1)}) &= -\sum_{k=1}^K \ddot{\sigma}_k^E \mathbf{s}^\dagger \mathbf{H}_{c,k}^\dagger \mathbf{v} \mathbf{v}^\dagger \mathbf{H}_{c,k} \mathbf{s} \\ &\quad 2\Re \left\{ \mathbf{v}^\dagger \mathbf{H}_t \mathbf{s} \right\} - \mathbf{v}^\dagger \mathbf{R}_n \mathbf{v}. \end{aligned} \quad (54)$$

It is seen that

$$\begin{cases} f_{\text{WAVE}}(\mathbf{s}; \mathbf{s}_{(m-1)}) \leq f(\mathbf{s}), \\ f_{\text{WAVE}}(\mathbf{s}_{(m-1)}; \mathbf{s}_{(m-1)}) = f(\mathbf{s}_{(m-1)}). \end{cases} \quad (55)$$

Based on (55), we have that

$$\begin{aligned} f(\mathbf{s}_{(m)}) &\geq f_{\text{WAVE}}(\mathbf{s}_{(m)}; \mathbf{s}_{(m-1)}) \geq f_{\text{WAVE}}(\mathbf{s}_{(m-1)}; \mathbf{s}_{(m-1)}) \\ &= f(\mathbf{s}_{(m-1)}), \end{aligned} \quad (56)$$

where  $f(\mathbf{s}_{(m)}) \geq f_{\text{WAVE}}(\mathbf{s}_{(m)}; \mathbf{s}_{(m-1)})$  comes from the first inequality in (56),  $f_{\text{WAVE}}(\mathbf{s}_{(m)}; \mathbf{s}_{(m-1)}) \geq f_{\text{WAVE}}(\mathbf{s}_{(m-1)}; \mathbf{s}_{(m-1)})$  results from the fact that  $\mathbf{s}_{(m)} = \arg \max_{\mathbf{s}} f_{\text{WAVE}}(\mathbf{s}; \mathbf{s}_{(m-1)})$ . Hence, it is obvious that  $f_{\text{WAVE}}(\mathbf{s}; \mathbf{s}_{(m-1)})$  provides a tight lower bound to  $f(\mathbf{s})$  at point  $\mathbf{s}_{(m-1)}$ .

It is seen that the objective is already a convex quadratic function and the non-convexity results from the modulus limitation. Note that the modulus constraint can be split into  $|s_l| \leq \sqrt{\frac{e_t}{L}}$  and  $|s_l| \geq \sqrt{\frac{e_t}{L}}$ , and the non-convexity comes from the latter, we aim to find convex approximation for it. It is easy to check that at any point  $\mathbf{s}_{(m-1)} \in \mathbb{C}^L$ ,  $2\Re \left\{ s_l^* s_{(m-1),l} \right\} - |s_{(m-1),l}|^2$  provides a lower approximation for  $|s_l|^2$ . However, potential infeasibility can be introduced after utilizing such approximation since the intersection of  $|s_l| \leq \sqrt{\frac{e_t}{L}}$  and  $2\Re \left\{ s_l^* s_{(m-1),l} \right\} - |s_{(m-1),l}|^2 \geq \frac{e_t}{L}$  only contains one element. To prevent this, inspired by the FPP idea [55], [56], [57], [58], we relax the

<sup>8</sup>We have omitted the function dependence on  $\phi^{(i-1)}$  for brevity with some abuse of notation since it remains constant in this part.

constraints by introducing a slack variable  $\eta \in \mathbb{C}^L$ . Specifically, the original problem can now be approximated by

$$\dot{\mathcal{P}}_{s,(m)} \left\{ \begin{array}{l} \max_{\mathbf{s}, \eta} f_{\text{WAVE}}(\mathbf{s}; \mathbf{s}_{(m-1)}) - \varsigma \|\boldsymbol{\eta}\|_2 \\ \text{s.t. } |s_l| \leq \sqrt{\frac{e_t}{L}}, l = 1, 2, \dots, L, \\ 2\Re \left\{ s_l^* s_{(m-1),l} \right\} - |s_{(m-1),l}|^2 \geq \frac{e_t}{L} - \eta_l, \\ l = 1, 2, \dots, L, \\ \|\mathbf{s} - \mathbf{s}_{\text{ref}}\|_2^2 \leq \delta \cdot e_t, \\ \mathbf{s}^\dagger \tilde{\mathbf{R}}_{\text{sum}} \mathbf{s} \leq e_{\text{sc}}, \\ \boldsymbol{\eta} \succeq 0, \boldsymbol{\eta}_{(m-1)} \succeq \boldsymbol{\eta}, \\ f_{\text{WAVE}}(\mathbf{s}; \mathbf{s}_{(m-1)}) \geq f(\mathbf{s}_{(m-1)}), \end{array} \right. \quad (57)$$

where  $\varsigma$  is a pre-defined penalty parameter and  $\eta$  is a non-negative slack variable. By sequentially updating  $\mathbf{s}$  through solving a series of problem  $\{\dot{\mathcal{P}}_{s,(m)}\}_{m=1}^\infty$ ,  $f(\mathbf{s})$  can be monotonically improved to convergence. The monotonically increasing property can be guaranteed by the fact that  $f(\mathbf{s}_{(m)}) \geq f_{\text{WAVE}}(\mathbf{s}_{(m)}; \mathbf{s}_{(m-1)}) \geq f(\mathbf{s}_{(m-1)})$ . Moreover, the employed FPP scheme can provide some guarantees on the property of the optimized solution. In particular, denote the optimized waveform vector at convergence by  $\mathbf{s}^{(i)}$ , then  $\mathbf{s}^{(i)}$  is a KKT point of  $\tilde{\mathcal{P}}_s^{(i)}$  [56], [58].

## APPENDIX C

## PROOF OF PROPOSITION 3

Note that  $\tilde{\Xi}$  can be equivalently cast as

$$\begin{aligned} \tilde{\Xi} &= \left\{ \tilde{\phi} \in \mathbb{C}^N \mid |\tilde{\phi}_n| = 1, \arg(\tilde{\phi}_{N+1}) \in \bar{\Phi}, \right. \\ &\quad \left. \arg(\tilde{\phi}_n) \in \Phi', n = 1, 2, \dots, N \right\}, \end{aligned} \quad (58)$$

where

$$\begin{aligned} \Phi' &= \left\{ \arg(\tilde{\phi}_{N+1}), \Delta\vartheta + \arg(\tilde{\phi}_{N+1}), \dots, \right. \\ &\quad \left. (N_{\text{RCV}} - 1) \Delta\vartheta + \arg(\tilde{\phi}_{N+1}) \right\}. \end{aligned} \quad (59)$$

On the other hand, when the phase of  $\tilde{\phi}_{N+1}$  is restricted within  $\bar{\Phi}$ , i.e.,  $\bar{\Phi} = \Phi$ , we can assume that  $\arg(\tilde{\phi}_{N+1}) = h \Delta\vartheta$  with  $h \in \{0, 1, \dots, (N_{\text{RCV}} - 1)\}$ . In this context, the specific form of  $\Phi'$  can be given as

$$\begin{aligned} \Phi' &= \{h \Delta\vartheta, (h+1) \Delta\vartheta, \dots, (N_{\text{RCV}} - 1 + h) \Delta\vartheta\} \\ &= \left\{ \frac{h}{N_{\text{RCV}}} 2\pi, \frac{h}{N_{\text{RCV}}} 2\pi + \frac{2\pi}{N_{\text{RCV}}}, \dots, \right. \\ &\quad \left. \frac{h}{N_{\text{RCV}}} 2\pi + \frac{(N_{\text{RCV}} - 1)}{N_{\text{RCV}}} 2\pi \right\}. \end{aligned} \quad (60)$$

An interesting fact of set  $\Phi'$  is that it also uniformly divides the range  $[\frac{h}{N_{\text{RCV}}} 2\pi, \frac{h}{N_{\text{RCV}}} 2\pi + 2\pi]$  into  $N_{\text{RCV}}$  discrete phases with interval  $\frac{2\pi}{N_{\text{RCV}}}$ , while the phase of a complex number is within  $[0, 2\pi]$ . This is equal to divide  $[0, 2\pi]$  with interval  $\frac{2\pi}{N_{\text{RCV}}}$  regardless of the actual value of  $h$ . In other words,  $\Phi'$  and  $\bar{\Phi}$  describes the same set when  $\bar{\Phi} = \Phi$ , which gives the equivalence between  $\tilde{\Xi}'$  and  $\tilde{\Xi}$ .

## ACKNOWLEDGMENT

The authors would like to thank Prof. Mojtaba Soltanalian and anonymous reviewers for their constructive comments on improving the quality of this paper.

## REFERENCES

- [1] M. Di Renzo et al., "Smart radio environments empowered by reconfigurable intelligent surfaces: How it works, state of research, and the road ahead," *IEEE J. Sel. Areas Commun.*, vol. 38, no. 11, pp. 2450–2525, Nov. 2020.
- [2] M. A. ElMossallamy, H. Zhang, L. Song, K. G. Seddik, Z. Han, and G. Y. Li, "Reconfigurable intelligent surfaces for wireless communications: Principles, challenges, and opportunities," *IEEE Trans. Cogn. Commun. Netw.*, vol. 6, no. 3, pp. 990–1002, Sep. 2020.
- [3] Y. Liu et al., "Reconfigurable intelligent surfaces: Principles and opportunities," *IEEE Commun. Surveys Tuts.*, vol. 23, no. 3, pp. 1546–1577, thirdquarter 2021.
- [4] Q. Wu and R. Zhang, "Towards smart and reconfigurable environment: Intelligent reflecting surface aided wireless network," *IEEE Commun. Mag.*, vol. 58, no. 1, pp. 106–112, Jan. 2020.
- [5] S. Zhang and R. Zhang, "Capacity characterization for intelligent reflecting surface aided MIMO communication," *IEEE J. Sel. Areas Commun.*, vol. 38, no. 8, pp. 1823–1838, Aug. 2020.
- [6] Y. Han, W. Tang, S. Jin, C.-K. Wen, and X. Ma, "Large intelligent surface-assisted wireless communication exploiting statistical CSI," *IEEE Trans. Veh. Technol.*, vol. 68, no. 8, pp. 8238–8242, Aug. 2019.
- [7] Q. Wu and R. Zhang, "Intelligent reflecting surface enhanced wireless network via joint active and passive beamforming," *IEEE Trans. Wireless Commun.*, vol. 18, no. 11, pp. 5394–5409, Nov. 2019.
- [8] Q. Wu and R. Zhang, "Beamforming optimization for wireless network aided by intelligent reflecting surface with discrete phase shifts," *IEEE Trans. Commun.*, vol. 68, no. 3, pp. 1838–1851, Mar. 2020.
- [9] J. Ye, S. Guo, and M.-S. Alouini, "Joint reflecting and precoding designs for SER minimization in reconfigurable intelligent surfaces assisted MIMO systems," *IEEE Trans. Wireless Commun.*, vol. 19, no. 8, pp. 5561–5574, Aug. 2020.
- [10] J. Mirza and B. Ali, "Channel estimation method and phase shift design for reconfigurable intelligent surface assisted MIMO networks," *IEEE Trans. Cogn. Commun. Netw.*, vol. 7, no. 2, pp. 441–451, Jun. 2021.
- [11] X. Tang, X. Lan, D. Zhai, R. Zhang, and Z. Han, "Securing wireless transmissions with RIS-receiver coordination: Passive beamforming and active jamming," *IEEE Trans. Veh. Technol.*, vol. 70, no. 6, pp. 6260–6265, Jun. 2021.
- [12] C. Huang, R. Mo, and C. Yuen, "Reconfigurable intelligent surface assisted multiuser MISO systems exploiting deep reinforcement learning," *IEEE J. Sel. Areas Commun.*, vol. 38, no. 8, pp. 1839–1850, Aug. 2020.
- [13] X. Wang, Z. Fei, J. Huang, and H. Yu, "Joint waveform and discrete phase shift design for RIS-assisted integrated sensing and communication system under Cramér-Rao bound constraint," *IEEE Trans. Veh. Technol.*, vol. 71, no. 1, pp. 1004–1009, Jan. 2022.
- [14] X. Wang, Z. Fei, Z. Zheng, and J. Guo, "Joint waveform design and passive beamforming for RIS-assisted dual-functional radar-communication system," *IEEE Trans. Veh. Technol.*, vol. 70, no. 5, pp. 5131–5136, May 2021.
- [15] K. Zhong, J. Hu, C. Pan, M. Deng, and J. Fang, "Joint waveform and beamforming design for RIS-aided ISAC systems," *IEEE Signal Process. Lett.*, vol. 30, pp. 165–169, 2023.
- [16] W. Zhong, Z. Yu, Y. Wu, F. Zhou, Q. Wu, and N. Al-Dhahir, "Resource allocation for an IRS-assisted dual-functional radar and communication system: Energy efficiency maximization," *IEEE Trans. Green Commun. Netw.*, vol. 7, no. 1, pp. 469–482, Mar. 2023.
- [17] Q. Zhu, M. Li, R. Liu, and Q. Liu, "Joint transceiver beamforming and reflecting design for active RIS-aided ISAC systems," *IEEE Trans. Veh. Technol.*, vol. 72, no. 7, pp. 9636–9640, Jul. 2023.
- [18] T. Wei, L. Wu, K. V. Mishra, and M. B. Shankar, "Multiple IRS-assisted wideband dual-function radar-communication," in *Proc. 2nd IEEE Int. Symp. Joint Commun. Sens. (JC&S)*, Piscataway, NJ, USA: IEEE Press, 2022, pp. 1–5.
- [19] T. Wei, L. Wu, K. V. Mishra, and M. B. Shankar, "RIS-aided wideband DFRC with reconfigurable holographic surface," in *Proc. IEEE Int. Conf. Acoust., Speech Signal Process. (ICASSP)*, Piscataway, NJ, USA: IEEE Press, 2023, pp. 1–5.
- [20] S. Yan, S. Cai, W. Xia, J. Zhang, and S. Xia, "A reconfigurable intelligent surface aided dual-function radar and communication system," in *Proc. 2nd IEEE Int. Symp. Joint Commun. Sens. (JC&S)*, Piscataway, NJ, USA: IEEE Press, 2022, pp. 1–6.
- [21] R. P. Sankar, B. Deepak, and S. P. Chepuri, "Joint communication and radar sensing with reconfigurable intelligent surfaces," in *Proc. IEEE 22nd Int. Workshop Signal Process. Adv. Wireless Commun. (SPAWC)*, Piscataway, NJ, USA: IEEE Press, 2021, pp. 471–475.
- [22] R. Liu, M. Li, H. Luo, Q. Liu, and A. L. Swindlehurst, "Integrated sensing and communication with reconfigurable intelligent surfaces: Opportunities, applications, and future directions," *IEEE Wireless Commun.*, vol. 30, no. 1, pp. 50–57, Feb. 2023.
- [23] W. Lu, B. Deng, Q. Fang, X. Wen, and S. Peng, "Intelligent reflecting surface-enhanced target detection in MIMO radar," *IEEE Sensors Lett.*, vol. 5, no. 2, pp. 1–4, Feb. 2021.
- [24] W. Lu, Q. Lin, N. Song, Q. Fang, X. Hua, and B. Deng, "Target detection in intelligent reflecting surface aided distributed MIMO radar systems," *IEEE Sensors Lett.*, vol. 5, no. 3, pp. 1–4, Mar. 2021.
- [25] S. Buzzi, E. Grossi, M. Lops, and L. Venturino, "Radar target detection aided by reconfigurable intelligent surfaces," *IEEE Signal Process. Lett.*, vol. 28, pp. 1315–1319, 2021.
- [26] S. Buzzi, E. Grossi, M. Lops, and L. Venturino, "Foundations of MIMO radar detection aided by reconfigurable intelligent surfaces," *IEEE Trans. Signal Process.*, vol. 70, pp. 1749–1763, 2022.
- [27] A. Aubry, A. De Maio, and M. Rosamilia, "Reconfigurable intelligent surfaces for N-LOS radar surveillance," *IEEE Trans. Veh. Technol.*, vol. 70, no. 10, pp. 10735–10749, Oct. 2021.
- [28] F. Wang, H. Li, and J. Fang, "Joint active and passive beamforming for IRS-assisted radar," *IEEE Signal Process. Lett.*, vol. 29, pp. 349–353, 2021.
- [29] L. Ran, S. Chen, and F. Xi, "Beampattern synthesis for active RIS-assisted radar with sidelobe level minimization," *Signal Process.*, vol. 206, 2023, Art. no. 108925.
- [30] E. Grossi and L. Venturino, "Beampattern design for radars with reconfigurable intelligent surfaces," in *Proc. IEEE Radar Conf. (RadarConf)*, Piscataway, NJ, USA: IEEE Press, 2023, pp. 1–6.
- [31] Z. Esmailbeig, K. V. Mishra, A. Eamaz, and M. Soltanalian, "Cramér-Rao lower bound optimization for hidden moving target sensing via multi-IRS-aided radar," *IEEE Signal Process. Lett.*, vol. 29, pp. 2422–2426, 2022.
- [32] Z. Esmailbeig, A. Eamaz, K. V. Mishra, and M. Soltanalian, "Joint waveform and passive beamformer design in multi-IRS-aided radar," in *Proc. IEEE Int. Conf. Acoust., Speech Signal Process. (ICASSP)*, Piscataway, NJ, USA: IEEE Press, 2023, pp. 1–5.
- [33] Z. Esmailbeig, K. V. Mishra, A. Eamaz, and M. Soltanalian, "IRS-aided radar: Enhanced target parameter estimation via intelligent reflecting surfaces," in *Proc. IEEE 12th Sensor Array Multichannel Signal Process. Workshop (SAM)*, Piscataway, NJ, USA: IEEE Press, 2022, pp. 286–290.
- [34] H. Zhang, H. Zhang, B. Di, K. Bian, Z. Han, and L. Song, "MetaRadar: Multi-target detection for reconfigurable intelligent surface aided radar systems," *IEEE Trans. Wireless Commun.*, vol. 21, no. 9, pp. 6994–7010, Sep. 2022.
- [35] R. Liu, M. Li, Y. Liu, Q. Wu, and Q. Liu, "Joint transmit waveform and passive beamforming design for RIS-aided DFRC systems," *IEEE J. Sel. Topics Signal Process.*, vol. 16, no. 5, pp. 995–1010, Aug. 2022.
- [36] R. Liu, M. Li, and Q. Liu, "Joint transmit waveform and reflection design for RIS-assisted MIMO radar systems," *IEEE Commun. Lett.*, vol. 27, no. 2, pp. 615–619, Feb. 2023.
- [37] Z. Esmailbeig, A. Eamaz, K. V. Mishra, and M. Soltanalian, "Moving target detection via multi-IRS-aided OFDM radar," in *Proc. IEEE Radar Conf. (RadarConf)*, Piscataway, NJ, USA: IEEE Press, 2023, pp. 1–6.
- [38] M. Rihan, E. Grossi, L. Venturino, and S. Buzzi, "Spatial diversity in radar detection via active reconfigurable intelligent surfaces," *IEEE Signal Process. Lett.*, vol. 29, pp. 1242–1246, 2022.
- [39] L. Wu, X. Cheng, H. Huang, D. Ciunozzo, B. Shankar, and B. Ottersten, "Constant-modulus waveform design with polarization-adaptive power allocation in polarimetric radar," *IEEE Trans. Signal Process.*, vol. 71, pp. 2146–2161, 2023.
- [40] L. Wu, P. Babu, and D. P. Palomar, "Transmit waveform/receive filter design for MIMO radar with multiple waveform constraints," *IEEE Trans. Signal Process.*, vol. 66, no. 6, pp. 1526–1540, Mar. 2018.
- [41] J. Yang, A. Aubry, A. De Maio, X. Yu, and G. Cui, "Multi-spectrally constrained transceiver design against signal-dependent interference," *IEEE Trans. Signal Process.*, vol. 70, pp. 1320–1332, 2022.



- [42] L. Wu, P. Babu, and D. P. Palomar, "Cognitive radar-based sequence design via SINR maximization," *IEEE Trans. Signal Process.*, vol. 65, no. 3, pp. 779–793, Feb. 2017.
- [43] G. Cui, A. De Maio, A. Farina, and J. Li, *Radar Waveform Design Based on Optimization Theory*. Rijeka, Croatia: SciTech, 2020.
- [44] S. M. Kay, *Fundamentals of Statistical Signal Processing*. Englewood Cliffs, NJ, USA: Prentice-Hall, 1993.
- [45] A. Aubry, A. De Maio, M. A. Govoni, and L. Martino, "On the design of multi-spectrally constrained constant modulus radar signals," *IEEE Trans. Signal Process.*, vol. 68, pp. 2231–2243, 2020.
- [46] A. Aubry, A. DeMaio, A. Farina, and M. Wicks, "Knowledge-aided (potentially cognitive) transmit signal and receive filter design in signal-dependent clutter," *IEEE Trans. Aerosp. Electron. Syst.*, vol. 49, no. 1, pp. 93–117, Jan. 2013.
- [47] Z. Xie, C. Fan, Z. Xu, J. Zhu, and X. Huang, "Robust joint code-filter design under uncertain target interpulse fluctuation," *Signal Process.*, vol. 201, 2022, Art. no. 108687.
- [48] Z. Xie, Z. Xu, S. Han, J. Zhu, and X. Huang, "Modulus constrained minimax radar code design against target interpulse fluctuation," *IEEE Trans. Veh. Technol.*, vol. 72, no. 10, pp. 13671–13676, Oct. 2023.
- [49] S. P. Boyd and L. Vandenberghe, *Convex Optimization*. Cambridge, U.K.: Cambridge Univ. Press, 2004.
- [50] Y. Sun, P. Babu, and D. P. Palomar, "Majorization-minimization algorithms in signal processing, communications, and machine learning," *IEEE Trans. Signal Process.*, vol. 65, no. 3, pp. 794–816, Feb. 2017.
- [51] J. Song, P. Babu, and D. P. Palomar, "Optimization methods for designing sequences with low autocorrelation sidelobes," *IEEE Trans. Signal Process.*, vol. 63, no. 15, pp. 3998–4009, Aug. 2015.
- [52] A. Ben-Tal and A. Nemirovski, *Lectures on Modern Convex Optimization (2012)*. Philadelphia, PA, USA: SIAM, 2012.
- [53] Z. Esmailbeig, K. V. Mishra, A. Eamaz, and M. Soltanalian, "Submodular optimization for placement of intelligent reflecting surfaces in sensing systems," in *2023 IEEE 9th Internat. Workshop Comput. Adv. in Multi-Sensor Adapt. Process. (CAMSAP)*, Herradura, Costa Rica, 2023, pp. 401–405.
- [54] E. Tohidi, S. Haesloop, L. Thiele, and S. Stańczak, "Near-optimal LoS and orientation aware intelligent reflecting surface placement," in *Proc. IEEE Int. Conf. Commun. (ICC)*, Piscataway, NJ, USA: IEEE Press, 2023, pp. 498–504.
- [55] X. Yu, H. Qiu, J. Yang, W. Wei, G. Cui, and L. Kong, "Multispectrally constrained MIMO radar beampattern design via sequential convex approximation," *IEEE Trans. Aerosp. Electron. Syst.*, vol. 58, no. 4, pp. 2935–2949, Aug. 2022.
- [56] X. Yu, K. Alhujaili, G. Cui, and V. Monga, "MIMO radar waveform design in the presence of multiple targets and practical constraints," *IEEE Trans. Signal Process.*, vol. 68, pp. 1974–1989, 2020.
- [57] Z. Xie, Z. Xu, C. Fan, S. Han, and X. Huang, "Robust radar waveform optimization under target interpulse fluctuation and practical constraints via sequential Lagrange dual approximation," *IEEE Trans. Aerosp. Electron. Syst.*, vol. 59, no. 6, pp. 9711–9721, Dec. 2023.
- [58] O. Mehanna, K. Huang, B. Gopalakrishnan, A. Konar, and N. D. Sidiropoulos, "Feasible point pursuit and successive approximation of non-convex QCQPs," *IEEE Signal Process. Lett.*, vol. 22, no. 7, pp. 804–808, Jul. 2015.



**Zhuang Xie** received the B.S. degree in electronic information engineering from Harbin Institute of Technology, Harbin, China, in 2018, and the M.S. degree in information and communication engineering from the National University of Defense Technology, Changsha, China, in 2020, where he is currently working toward the Ph.D. degree. His research interests include radar signal processing and optimization theory, with emphasis on radar waveform design.



**Linlong Wu** (Senior Member, IEEE) received the B.E. degree in electronic information from Xi'an Jiaotong University (XJTU), Xi'an, China, in 2014, and the Ph.D. degree in electronic and computer engineering from Hong Kong University of Science and Technology (HKUST), Hong Kong, in 2018. From November 2018 to October 2020, he was with the wireless network group of Alibaba Cloud as a Research Engineer working on designing and building commercial RFID-based localization systems. Since November 2020, he has been with the Interdisciplinary Centre for Security, Reliability and Trust (SnT), University of Luxembourg, and he is currently a Research Scientist with the Signal Processing Applications in Radar and Communications (SPARC) Group. His research interests include signal processing, optimization, and machine learning with applications in waveform design, integrated sensing and communication, and IoT networks.



**Jiahua Zhu** (Senior Member, IEEE) received the B.S. degree in electronic engineering and the Ph.D. degree in information and communication engineering from the National University of Defense Technology, Changsha, China, in 2012 and 2018, respectively. He is currently an Associate Professor and the Master's Supervisor with the College of Meteorology and Oceanography, National University of Defense Technology. From November 2015 to November 2017, he was a Visiting Ph.D. Student with the School of Engineering, RMIT University, and the Department of Electrical and Electronic Engineering, University of Melbourne, Australia. His current research interests include waveform design and target detection for radar and sonar. He received the Best Paper Award in The 9th Research Symposium for Chinese Ph.D. Students and Scholars in Australia, 2016, the Excellent Paper Award in 2021 IEEE/OES China Ocean Acoustics Conference, and the outstanding Ph.D. degree thesis of the Chinese People's Liberation Army (PLA), 2020. He is a Program Co-Chair and Regional Chair of IEEE International Conference on Signal and Image Processing (ICSIP), an Editorial Board Member of *IET Signal Processing*, a Topical Advisory Panel Member and the Lead Guest Editor of *Remote Sensing*, and the Guest Editor of IEEE JOURNAL OF SELECTED TOPICS IN APPLIED EARTH OBSERVATIONS AND REMOTE SENSING.



**Marco Lops** (Fellow, IEEE) received the Laurea and Ph.D. degree from "Federico II" University. Previously, he was an Assistant Professor and then became an Associate Professor with the University of Naples Federico II. In March 2000, he moved to the University of Cassino and Southern Lazio as a Full Professor and he returned to the University of Naples Federico II in 2018. From 2009 to 2012, he was also with ENSEEIHT, Toulouse, France, first as a Full Professor (on leave of absence from Italy) and then as a Visiting Professor. In Fall 2008, he was a Visiting Professor with the University of Minnesota and Columbia University, in Spring 2009. Previously, he had also held visiting positions with the University of Connecticut, Rice University, and Princeton University. He is currently a Professor with the Department of Electrical and Information Technology (DIETI), University of Naples Federico II, Italy. He has authored or co-authored more than 90 scientific papers published on refereed journals. His research interests include detection and estimation, with emphasis on communications and radar signal processing. He was a co-recipient (with Ezio Biglieri) of the 2014 Best Paper Award from the *Journal of Communications and Networks*. From 2009 to 2015, he served two terms for the Sensor Array and Multichannel Signal Processing Technical Committee (SAM). He has served as an Associate Editor for the *Journal of Communications and Networks*, IEEE TRANSACTIONS ON INFORMATION THEORY (Area: Detection and Estimation, two terms), IEEE SIGNAL PROCESSING LETTERS, and IEEE TRANSACTIONS ON SIGNAL PROCESSING (two terms). He also served as a Senior Area Editor for IEEE TRANSACTIONS ON SIGNAL PROCESSING. He was selected to serve as a Distinguished Lecturer for the Signal Processing Society from 2018 to 2020.



**Xiaotao Huang** (Senior Member, IEEE) received the B.S. and Ph.D. degrees in information and communications engineering from the National University of Defense Technology, Changsha, China, in 1990 and 1999, respectively. He is currently a Professor with the National University of Defense Technology. His research interests include radar theory, signal processing, and radio frequency signal suppression.



**M. R. Bhavani Shankar** (Senior Member, IEEE) received the master's and Ph.D. degree in electrical communication engineering from the Indian Institute of Science, Bangalore, in 2000 and 2007, respectively. He was a Postdoc with the ACCESS Linnaeus Centre, Signal Processing Laboratory, Royal Institute of Technology (KTH), Sweden, from 2007 to September 2009. In October 2009, he joined SnT as a Research Associate, and he is currently an Assistant Professor leading the Signal Processing Applications in Radar and Communications (SPARC) Group. From 2006 to 2007, he was with Beceem Communications, Bangalore, as a Staff Design Engineer working on physical layer algorithms for WiMAX compliant chipsets. He was a Visiting Student with the Communication Theory Group, ETH Zurich, headed by Prof. Helmut Bölcskei in 2004. Prior to joining Ph.D. degree, he worked on audio coding algorithms with Sasken Communications, Bangalore as a Design Engineer, from 2000 to 2001. His research interests include design and optimization of MIMO communication systems, automotive radar and array processing, polynomial signal processing, satellite communication systems, resource allocation, game theory, and fast algorithms for structured matrices. He is currently on the Executive Committee of the IEEE Benelux joint chapter on Communications and Vehicular Technology. He serves as a Handling Editor for Elsevier *Signal Processing*. He was a co-recipient of the 2014 Distinguished Contributions to Satellite Communications Award, from the Satellite and Space Communications Technical Committee of the IEEE Communications Society.